Geometry versus growth: internal consistency of the fla Lambda CDM model with KiDS-1000

Ruiz-Zapatero, J.; Stölzner, B.; Joachimi, B.; Asgari, M.; Bilicki, M.; Dvornik, A.; ... ; Wright, A.H.

Geometry vs growth

Internal consistency of the flat ΛCDM model with KiDS-1000

J. Ruiz-Zapatero[1,2], Benjamin Stölzner[2], Benjamin Joachimi[2], Marika Asgari[3], Maciej Bilicki[4], Andrej Dvornik[5], Benjamin Giblin[3], Catherine Heymans[3,5], Hendrik Hildebrandt[5], Arun Kannawadi[6], Konrad Kuijken[7], Tilman Tröster[3], Jan Luca van den Busch[5], and Angus H. Wright[5]

[1] University of Oxford, Denys Wilkinson Building, Keble Road, Oxford, OX1 3RH, UK
e-mail: `jaime.ruiz-zapatero@physics.ox.ac.uk`,
[2] Department of Physics and Astronomy, University College London, Gower Street, London WC1E 6BT, UK
[3] Institute for Astronomy, University of Edinburgh, Royal Observatory, Blackford Hill, Edinburgh, EH9 3HJ, UK
[4] Center for Theoretical Physics, Polish Academy of Sciences, al. Lotników 32/46, 02-668, Warsaw, Poland
[5] Ruhr University Bochum, Faculty of Physics and Astronomy, Astronomical Institute (AIRUB), German Centre for Cosmological Lensing, 44780 Bochum, Germany
[6] Department of Astrophysical Sciences, Princeton University, 4 Ivy Lane, Princeton, NJ 08544, USA
[7] Leiden Observatory, Leiden University, P.O.Box 9513, 2300RA Leiden, The Netherlands

Received –; accepted —

ABSTRACT

We carry out a multi-probe self-consistency test of the flat ΛCDM model with the aim of exploring potential causes of the reported tensions between high- and low-redshift cosmological observations. We divide the model into two theory regimes determined by the smooth background (geometry) and the evolution of matter density fluctuations (growth), each governed by an independent set of ΛCDM cosmological parameters. This extended model is constrained by a combination of weak gravitational lensing measurements from the the Kilo-Degree Survey, galaxy clustering signatures extracted from Sloan Digital Sky Survey campaigns and the Six-Degree Field Galaxy Survey, as well as the angular baryon acoustic scale and the primordial scalar fluctuation power spectrum measured in *Planck* cosmic microwave background (CMB) data. For both the weak lensing data set individually and the combined probes, we find strong consistency between the geometry and growth parameters, and with the posterior of standard ΛCDM analysis. Tension in the amplitude of matter density fluctuations as measured by the parameter S_8 persists at around 3σ, with a 1.5 % constraint of $S_8 = 0.776^{+0.016}_{-0.008}$ for the combined probes. We also observe less significant trends (at least 2σ) towards higher values of the Hubble constant $H_0 = 70.5^{+0.7}_{-1.5}\,\mathrm{km\,s^{-1}Mpc^{-1}}$ and towards lower values of the total matter density parameter $\Omega_\mathrm{m} = 0.289^{+0.007}_{-0.005}$ compared to the full *Planck* analysis. Including the subset of the CMB information in the probe combination enhances these differences rather than alleviate them, which we link to the discrepancy between low and high multipoles in *Planck* data. Our analysis does not yet yield clear signs whether the origin of discrepancies lies in ΛCDM structure growth or expansion history, but holds promise as an insightful test for forthcoming more powerful data.

Key words. cosmological parameters – methods: data analysis – cosmology: theory – large-scale structure of Universe – gravitational lensing: weak

1. Introduction

The dramatic increase of precision experienced by cosmology over the last thirty years has recently led to the discovery of potential inconsistencies in our cosmological model that previously might have been obscured by statistical errors. One of the most relevant of these inconsistencies is the apparent discrepancy between a subset of the free parameters of the concordance ΛCDM model (Condon & Matthews 2018; Lahav & Liddle 2019) measured at early and late times of the Universe. The most notable manifestation of this tension is the 4.2σ (Riess et al. 2021) difference in the value of the Hubble constant, H_0, between distance ladder estimates and the early-Universe cosmic microwave background (CMB) probe *Planck* (Planck Collaboration et al. 2020a). Moreover, late-Universe probes of the large-scale structure, such as weak gravitational lensing (WL) and galaxy clustering, prefer a lower amplitude of the growth of structure than *Planck*,

with tension up to 3.2σ level in the parameter $S_8 = \sigma_8\sqrt{\frac{\Omega_\mathrm{m}}{0.3}}$, where σ_8 is the standard deviation of matter density fluctuations in spheres of radius $8\,h^{-1}\mathrm{Mpc}$ today and Ω_m is the matter density parameter (Alsing et al. 2017; Joudaki et al. 2017a; Loureiro et al. 2019; Asgari et al. 2021; Tröster et al. 2020b; Kobayashi et al. 2020).

If confirmed, the reasons behind these discrepancies could be twofold. On the one hand, if we assume our cosmological theory to be correct, the origin of the tension must lie in the data or their analysis of either set of probes. On the other hand, if we decide to trust the current measurements, the tension would be suggestive of a shortcoming of the theory used to analyse the aforementioned data, such as new physics beyond the standard model (e.g. Mörtsell & Dhawan 2018; Capistrano et al. 2020; Abellan et al. 2020).

Numerous efforts have been made to identify possible errors in the respective data analysis processes of each set of probes.

Concerning the local measurements of the Hubble parameter, examples of these efforts can be found in the most recent review of the distance ladder (Riess et al. 2021). Large-scale structure surveys have also carried out extensive systematics checks and internal consistency tests; see Abbott et al. (2018a); Lemos et al. (2020) and Doux et al. (2021) for the Dark Energy Survey, Köhlinger et al. (2019); Wright et al. (2020); van den Busch et al. (2020); Giblin et al. (2021); Asgari et al. (2021) and Hildebrandt et al. (2021) for the Kilo-Degree Survey (KiDS), and Laurent et al. (2017) and Vargas-Magaña et al. (2018) for the Baryon Oscillation Spectroscopic Survey (BOSS) and the Extented Baryon Oscillation Spectroscopic Survey (eBOSS) respectively. As for the CMB probes, Efstathiou & Gratton (2019) undertook a thorough revision of the CamSpec Likelihood used to analyze *Planck* data in search for potential sytematics. Moreover, the initiative 'Beyond *Planck*' is currently conducting a thorough revision of *Planck*'s and WMAP's methodology (BeyondPlanck Collaboration et al. 2020). However, no known systematic errors that could convincingly explain either tension have been reported yet. Equally, the tensions have proven not to be relieved by combining data of independent late-Universe probes (e.g. Abbott et al. 2018b; Tröster et al. 2020b; Heymans et al. 2021) nor by proposing alternative ways of measuring the Hubble parameter locally (e.g. Freedman et al. 2019; Pesce et al. 2020).

In this work we develop and apply methodology to test the self-consistency of the spatially flat ΛCDM model with the goal of providing guidance as to which regime of the theory could drive the observed tension. To do so, we differentiate between two theory regimes within the cosmological model: *geometry*, i.e. parts of the model related to the dynamics of the smooth space-time lattice; and *growth*, concerning the formation of matter anisotropies on top of the dynamics of the space-time lattice. The key distinguishing factor between the two regimes is that *geometry* fully operates within the assumptions of homogeneity and isotropy while *growth* considers perturbations on this background. If the ΛCDM model is self-consistent, the same set of cosmological parameter values should correctly reproduce both of its theory regimes. We test this assumption by letting each theory regime be governed by an independent set of ΛCDM parameters. Then, we employ a range of high- and low-redshift cosmological probes to obtain constraints for each regime of the theory. Any discrepancies between the pairs of *geometry* and *growth* parameters would hint at the origin of potential failures in our current cosmological model.

This approach, in the particular formulation we use in this work, was originally proposed by Ruiz & Huterer (2015). However, our interpretation of *geometry* and *growth* lies closer to that put forward by Nesseris & Perivolaropoulos (2007). Similar studies were conducted prior to this publication which also explore the effects of splitting certain parameters of a given cosmological model as a means to investigating its self-consistency. As early as 2004, Chu & Knox (2005) studied the consistency of the constraints coming from data on the ionization history and on the pressure profile of the pre-recombination fluid in the context of flat ΛCDM by duplicating the baryon density parameter, Ω_b, and allowing each instance be constrained by one of the phenomena. In Abate & Lahav (2008) a similar exercise was performed on the total matter density parameter, Ω_m, by having three instances, each controlled by a different physical observable in SN Ia data.

Beyond ΛCDM, Bernal et al. (2016) and Wang et al. (2007) undertook multi-probe studies of the consistency of the wCDM model by splitting the equation-of-state parameter w, and the density parameter Ω_{DE}, of dark energy into their *geometry*

and *growth* contributions. During the final stages of our study, Muir et al. (2021) published a closely analogous investigation of geometry–growth consistency using several probes from the Dark Energy Survey in combination with external data. Our work is complementary in that it employs a different mix of data sources: weak gravitational lensing data from KiDS-1000 (Asgari et al. 2021), galaxy clustering data from BOSS (Alam et al. 2017) and the 6 Degree Field Galaxy Survey (6dFGS; Beutler et al. 2011), Lyman-α and quasar clustering information from the Extended Baryon Oscillation Spectroscopic Survey (eBOSS; de Sainte Agathe et al. 2019; Blomqvist et al. 2019), and subsets of the *Planck* CMB temperature and polarization anisotropy correlations. Moreover, our split is more comprehensive in that we duplicate the full flat-ΛCDM parameter space, whereas Ruiz & Huterer (2015) and Muir et al. (2021) limited themselves to a split in the dark matter density parameter only.

This work is structured as follows: in Section 2 we present the methodology of this work regarding the distinction between *geometry* and *growth* in the ΛCDM model and the resulting modelling of the observables of interest. In Section 3 we describe the data sets that we analyse. We discuss the likelihood analysis in Section 4 and present results in Section 5. In Section 6 we summarise our findings and conclude.

2. Methodology

2.1. Distinguishing geometry and growth

We adopt a classification of the theory of the ΛCDM model based on whether it keeps, or departs from, the assumptions of homogeneity and isotropy. These assumptions strictly prohibit the formation of structure in the universe. Hence, any information regarding the formation of structure in the model can be traced to where it departs from a smooth background. Thus, we distinguish two theoretical regimes: on the one hand, an isotropic, homogeneous background that describes the curvature and expansion history of the Universe, and on the other hand, a theory of perturbations that build up from the background and create the structures in the Universe[1]. We refer to these two regimes of the theory as *geometry* and *growth*, respectively.

In mathematical terms the departure from, or conservation of, homogeneity and isotropy can be fully encapsulated in the choice of metric since its shape is fully determined by the assumptions that we make about the universe which we aim to describe. Furthermore, the fundamental role that the metric plays in Einstein gravity means that these assumptions propagate into the entirety of the theoretical predictions of the model. Of these predictions, we particularly focus on two: the field equations, which describe the relationship between matter and gravity, and the equations of motion of the stress-energy tensor fields, which describe how the content of the Universe evolves over time. The FLRW line element, in which the assumptions of homogeneity and isotropy are expressed, directly leads to the Friedmann field equations. Moreover, the Friedmann field equations can be combined into a conservation law for the field that describes its evolution. The perturbation of this homogeneous background metric ultimately leads to the Jeans equation, describing the evolution of matter density perturbations over cosmic time (e.g. Baker et al. 2014).

---

[1] As in standard structure formation theory, we assume here that structure growth does not feed back significantly on the expansion history; see Clarkson et al. (2011) for a detailed discussion about this backreaction.

This dualistic understanding of the theory is extremely useful when calculating predictions of astrophysical phenomena. This is due to the fact that some phenomena can be accurately modelled purely within a particular regime. Thus, we can equivalently distinguish between *geometry* and *growth* observables as well as *geometry* and *growth* theory regimes. Furthermore, the modelling of more "complex" observables might need a combination of background and perturbation physics.

Nonetheless, if the ΛCDM model is to be self-consistent, both regimes of the theory must be governed by the same set of parameters, and therefore, parameter constraints based on *geometry* observables should be consistent with those from *growth* ones. Similarly, observables whose modelling makes use of both theory regimes should exhibit internal consistency between the preferred parametrizations of their different calculation stages.

In this work we test the self-consistency of the ΛCDM model by assigning to each theory regime its own set of cosmological parameters and simultaneously parametrizing them using a set of *geometry* and *growth* observables. This allows us to observe the parametrization preferences of each regime such that potential discrepancies can be identified. From here on we denote the sets of parameters governing the *geometry* and *growth* regimes of the theory as p^{geom} and p^{grow}, respectively. In this analysis we sample over the following parameters: $S_8 = \sigma_8 \sqrt{\Omega_{\mathrm{m}}/0.3}$; where σ_8 is the root-mean-square of matter density fluctuations in spheres of $8\,h^{-1}\mathrm{Mpc}$ and Ω_{m} is the total matter density parameter, the reduced Hubble parameter $h = H_0/(100\,\mathrm{km\,s^{-1}Mpc^{-1}})$, the reduced cosmological cold dark matter density $\omega_{\mathrm{cdm}} = \Omega_{\mathrm{cdm}}h^2$, the reduced cosmological baryonic density $\omega_{\mathrm{b}} = \Omega_{\mathrm{b}}h^2$ and the spectral index n_{s}.

We expect there to be correlations between p^{geom} and p^{grow} because one can fully derive the *growth* aspects from the *geometry* parameters and vice versa, via the Jeans equation, in cosmological models in which gravitational collapse is quasistatic up to the linear level of the theory (Silvestri et al. 2013; Baker et al. 2014). An explicit demonstration of this duality in GR+ΛCDM can be found in Alam et al. (2009). Thus, simply splitting the parameter space into two subsets does not ensure independent constraints for the two theory regimes. Moreover, even if the set of *geometry* cosmological parameters cannot constrain parameters that explicitly relate to matter anisotropies (e.g., S_8), fixing them would misrepresent this lack of constraining power. An analogous argument can be made for *growth* parameters that primarily affect the expansion history, such as h. We therefore assign the same, uninformative priors to both parameter sets and vary the full set in each case.

There are alternative interpretations of the categories of *geometry* and *growth* and that the choice made in this work is not necessarily unique. For example, in Muir et al. (2021) *growth* is limited to describe only the late, non-linear growth of structure based on the made argument that *geometry* and *growth* are analytically linked at the level of linear theory. These approaches are not contradictory but the different analysis choices prevent direct comparisons between the resulting constraints.

For the purposes of this work we limit ourselves to a spatially flat ΛCDM model. In agreement with Hildebrandt et al. (2020), we also assume two massless neutrino species and a third massive species with mass $m_{\mathrm{ncdm}} = 0.06\,\mathrm{eV}/c^2$, as well as a temperature of the non-cold relic $T_{\mathrm{ncdm}} = 0.71611\,\mathrm{K}$.

Table 1. *Geometry* and *growth* classification of the observables used in our analysis.

Geometry	Growth
BAO angular scale	RSD growth rate
WL lensing efficiencies	WL matter power spectrum
CMB first acoustic peak position	CMB primordial power spectrum

Notes. The first row lists features extracted from clustering signals (BAO: baryon acoustic oscillations; RSD: redshift space distortions), the second row weak lensing (WL) signal contributions, and the third row quantities inferred from cosmic microwave background (CMB) measurements.

2.2. Cosmological observables

In this section we introduce the physical observables used in this work, including a discussion of their *geometry* versus *growth* treatment; see Table 1 for an overview.

2.2.1. Weak lensing

In general relativity mass induces in its surrounding space-time a non-Euclidean geometry. In agreement with Fermat's principle, photons seek the path of least action through the curved space. These paths correspond to geodesic lines which are not straight in a Euclidean sense, thus causing light rays to appear bent. This deflection of light rays leads to similar observational effects as those of optical lenses, focusing and distorting the images we observe of celestial bodies that lie behind the lens. The effect of such lenses is usually quite weak, so that it can only be detected via statistical methods from large galaxy samples. This is referred to as weak lensing (WL).

Weak lensing measurements are an excellent tool to inspect the interplay between the different regimes of ΛCDM because it is sensitive to both *geometry* and *growth*. This is because the strength of the light deflection depends on the distances between the light source, the lens, and the observer, as well as the spatial distribution of the lenses and their density contrast with respect to the mean matter distribution. Formally, this duality can be observed in the key quantity of weak lensing, the lensing convergence κ (e.g. Bartelmann & Schneider 2001),

$$\kappa^i(\boldsymbol{\theta}) = \frac{3H_0^2\Omega_{\mathrm{m}}}{2c^2} \int_0^{\chi_{\mathrm{lim}}} \frac{\mathrm{d}\chi\,\chi}{a(\chi)} g^i(\chi)\delta(\chi\boldsymbol{\theta},\chi)\,, \tag{1}$$

where we assume a spatially flat universe. Here, χ is the radial comoving distance, χ_{lim} is the radial comoving distance to the horizon, a is the scale factor, c is the speed of light in the vacuum, and $\boldsymbol{\theta}$ is a two-dimensional vector that represents angular position on the sky. We also introduce the matter density contrast δ measured at a position and epoch determined by the comoving distance and the angular position. The lensing efficiency $g^i(\chi)$ is defined as

$$g^i(\chi) = \int_\chi^{\chi_{\mathrm{lim}}} \mathrm{d}\chi'n^i(\chi')\frac{\chi'-\chi}{\chi'}\,, \tag{2}$$

where $n^i(\chi')$ is the comoving distance distribution of source galaxies on which the lensing effect is measured, assigned to a tomographic redshift bin labelled by i. In practice, we measure the source distribution of redshifts, $n^i(z) = n^i(\chi)\,\mathrm{d}\chi/\mathrm{d}z$.

Since the effects of weak lensing are not strong enough to be directly observable, it is only possible to appreciate them statistically. The standard baseline two-point statistic to model weak lensing signals is the Fourier transform of the two-point correlation of the convergence across redshift bins i and j, the convergence power spectrum

$$C_\kappa^{ij}(\ell) = \frac{9}{4}\Omega_m^2 \left(\frac{H_0}{c}\right)^4 \int_0^{\chi_{lim}} d\chi \frac{g^i(\chi)g^j(\chi)}{a^2(\chi)} P_\delta\left(\frac{\ell+1/2}{\chi},\chi\right), \quad (3)$$

where $P_\delta(k,\chi)$ is the (non-linear) matter power spectrum evaluated at wavenumber k and an epoch marked by χ. In Eq. (3) the Limber approximation was applied (Limber 1953).

Angular power spectra are not directly measurable from a restricted survey footprint. We employ band powers derived from angular correlation function measurements; see Joachimi et al. (2021); van Uitert et al. (2018); Schneider et al. (2002) for a detailed description. Band powers can be modelled as linear functionals of the angular convergence power spectra,

$$C_{E,l}^{ij} = \frac{1}{2N_l} \int_0^\infty d\ell\,\ell\, W_{EE}^l(\ell)\, C_\kappa^{ij}(\ell), \quad (4)$$

for a band indexed by l, where the filter function W_{EE}^l is given by equation 26 of Joachimi et al. (2021). The normalisation, N_l, is defined such that the band powers trace $\ell^2 C_\kappa(\ell)$ at the logarithmic centre of the bin, $N_l = \ln(\ell_{up,l}) - \ln(\ell_{lo,l})$ with $\ell_{up,l}$ and $\ell_{lo,l}$ defining the edges of the top-hat band selection function for the bin indexed by l. Here, we have assumed that the model does not predict any B-modes, and we will only use the E-mode band powers in our analysis. This assumption is based on the work of Giblin et al. (2021) who showed that there is no significant detection of B-modes in KiDS-1000.

It is possible to establish a classification of the quantities that enter the convergence power spectrum as *geometry*- or *growth*-related. On the one hand, the cosmological dependence of the matter power spectrum P_δ is *growth*-related. On the other hand, the lensing efficiency solely concerns angular diameter distances (or comoving distances when assuming a flat universe), which are purely *geometry*-related. A more ambiguous decision is whether to consider the prefactor in Eq. (3) *geometry* or *growth*. This is due to the fact that, while these terms originate from the Poisson equation that relates the gravitational potential to its source, δ, in the context of the calculation of the observable they effectively contribute a simple distance relationship that does not necessarily regard anisotropies. In agreement with the criteria of recent work (Muir et al. 2021), we consider these prefactors as *geometry*.

2.2.2. Baryon acoustic oscillations

Baryon acoustic oscillations (BAOs) cause matter overdensities at a characteristic physical separation scale which corresponds to the size of the sound horizon at the end of the drag epoch, $r_s(z_d)$ (Peebles & Yu 1970; Hu & Dodelson 2002). The sound horizon is defined as the distance a pressure wave can travel from its time of emission in the very early Universe up to a given redshift. This can be expressed as

$$r_s(z) = \int_z^\infty \frac{c_s\, dz'}{H(z')}, \quad (5)$$

where c_s denotes the speed of sound, and where $H(z)$ is the expansion rate at redshift z. The end of the drag epoch is defined

as the time when photon pressure can no longer prevent gravitational instability in baryons around $z \sim 1020$ (Komatsu et al. 2009). The redshift of this time is typically estimated using the following fitting formula:

$$z_d = \frac{1291(\omega_m)^{0.251}}{1 + 0.659(\omega_m)^{0.828}}[1 + b_1(\omega_b)^{b_2}], \quad (6)$$

where $b_1 = 0.313(\omega_m)^{-0.419}[1 + 0.607(\omega_m)^{0.674}]$, $b_2 = 0.238(\omega_m)^{0.223}$ and $\omega_m = \omega_{cdm} + \omega_b$ is the reduced cosmological matter density; see Komatsu et al. (2009).

Since the overdensity manifests anisotropically in redshift-space as a three-dimensional shell around a given tracer, it is possible to shift the BAO peak position with respect to its position in a fiducial cosmology, parallel and perpendicular to the line of sight. Perpendicular to the line of sight, the BAO feature informs the trigonometric relationship

$$\theta \approx \frac{r_s(z)}{D_M(z)}, \quad (7)$$

where θ is the angle under which the scale of the sound horizon is observed, and $D_M(z)$ is the comoving angular diameter distance to redshift z, which in a flat universe is identical to the comoving radial distance $\chi(z)$. Parallel to the line of sight, the BAO feature allows us to measure the expansion history of the Universe. The BAO measurements along the line of sight can be use to constrain the relationship $H(z)r_s(z_d)$.

We cast our BAO measurements in the form of the dimensionless ratios (Alam et al. 2017; du Mas des Bourboux et al. 2020; de Sainte Agathe et al. 2019; Blomqvist et al. 2019):

$$\alpha_\parallel = \frac{[D_H/r_s(z_d)]}{[D_H/r_s(z_d)]_{fid}}; \quad \alpha_\perp = \frac{[\chi/r_s(z_d)]}{[\chi/r_s(z_d)]_{fid}}, \quad (8)$$

to describe shifts perpendicular and parallel to the line of sight, where $D_H(z) = c/H(z)$ is the Hubble distance and the label 'fid' denotes a quantity evaluated at the aforementioned fiducial cosmology. Nonetheless, the quantities chosen to represent these parallel and perpendicular signatures of the BAO feature can vary from probe to probe.

It is also common to combine the perpendicular and parallel information in the volume-averaged angular diameter distance defined as

$$D_v(z) = \left(\frac{cz}{H(z)}\chi^2(z)\right)^{1/3}, \quad (9)$$

or in the anisotropy parameter known as the Alcock-Paczynski parameter ; $F_{AP}(z)$ (Alcock & Paczynski 1979), defined as:

$$F_{AP}(z) = \chi(z)H(z)/c. \quad (10)$$

Although BAOs are a consequence of structure growth, their signature in the matter distribution can be translated into distance relationships that can be calculated without making use of density perturbations. This can be seen in the fact that, while the speed of propagation of BAOs, and thus the sound horizon, is a function of the matter content of the Universe, it can be completely calculated by assuming this content to be homogeneous and isotropic. Therefore, measurements of the position of the BAO peak in the CMB or in the large-scale structure can be classified as pure *geometry* phenomena.

2.2.3. Redshift space distortions

Redshift space distortions (RSDs) are modifications to the observed redshift of a given object due to its peculiar velocity along the line of sight on top of the recession velocity due to cosmological expansion (Kaiser 1987). RSDs are determined by peculiar motion in the gravitational potential of the surrounding matter distribution and thus governed by the Poisson equation, which makes them a pure *growth* effect. For galaxies on large, linear scales RSDs are dominated by the infall towards overdense structure, known as the Kaiser effect (Hamilton 1998).

Clustering two-point statistics as a function of transverse and line-of-sight separation can be used to extract RSDs via the quantity (e.g. Beutler et al. 2017)

$$f\sigma_8 \equiv \frac{d \ln \delta}{d \ln a} \sigma_8 , \qquad (11)$$

where f is the growth rate and δ is again the matter density contrast. Both f and σ_8 are evaluated at the effective redshift of the measurement, as opposed to the use of σ_8 in weak lensing which is always interpreted at $z = 0$.

2.2.4. Early-Universe geometry and growth parameters

The CMB is the richest source of cosmological information to date and particularly valuable as a complement to low-redshift probes of the large-scale structure. While a full re-analysis of *Planck* data is beyond the scope of this work, we would still like to make use of readily accessible CMB information that can be allocated cleanly to either the *geometry* or *growth* regimes. The primary CMB anisotropies can be described by a set of five cosmological parameters (Vonlanthen et al. 2010; Kosowsky et al. 2002): the reduced baryon density parameter ω_b, the reduced cold dark matter density parameter ω_{cdm}, the amplitude and spectral index of primordial scalar fluctuations, A_s and n_s respectively, and the angle subtended by the sound horizon at end of recombination epoch θ^* (cf. Eq. 7, evaluated at redshift $z^* \sim 1100$ as opposed to $z_d \sim 1020$). A detailed discussion of the role of each of these parameters in determining the physical properties of the CMB can be found in Mukhanov (2004).

The parameters n_s and A_s are pure *growth* quantities as they determine the primordial scalar fluctuation power spectrum

$$P_{\delta,\text{prim}}(k) = A_s \left(\frac{k}{k_0} \right)^{n_s} , \qquad (12)$$

where k_0 is the pivot scale of the power spectrum here set to the value of 0.05 Mpc^{-1} for consistency with *Planck* (Planck Collaboration et al. 2020a). In contrast, θ^* is clearly a parameter solely concerned with the background cosmology as it relates the distance to the surface of last scattering to the size of the sound horizon.

The roles of ω_b and ω_{cdm} are not readily categorised. On the one hand, they play a role in determining the relative height of the CMB peaks, related to density fluctuations, but they also govern the expansion history and the value of the speed of sound in the baryon-photon fluid, all describable in a smooth universe. Therefore we decided not to include CMB constraints on ω_b and ω_{cdm} in our analysis, but do make use of the marginalised posteriors of the combination $\{n_s, A_s, \theta^*\}$, taking their correlation into account. We note that similar analyses (Muir et al. 2021) have employed the CMB shift parameter $\mathcal{R}$, a measure of the change of location of the first power spectrum peak with respect to a fiducial cosmology (Efstathiou & Bond 1999). While the

$\mathcal{R}$ parameter is a good alternative to constrain *geometry*, in this work we decided to use θ^* as it is a direct analogue of quantities available for the large-scale structure BAO measurements. The parameter n_s can be directly matched to the sampled n_s values in our analysis to constrain *growth*. A_s can be inferred from the sampled S_8 value to constrain *growth*. On the other hand, we treat θ^* as another evaluation of the distance relationship in Eq. (7) and use it to constrain the *geometry* regime.

3. Data Sets

To constrain the *geometry* and *growth* regimes of ΛCDM, we jointly analyse a range of recent measurements. A summary of the data sets employed in this work is given in Table 2.

3.1. KiDS-1000 cosmic shear measurements

We employ cosmic shear measurements from the fourth data release of the European Southern Observatory's Kilo Degree Survey (KiDS; Kuijken et al. 2019) incorporating data from the fully overlapping VISTA Kilo-Degree Infrared Galaxy Survey (VIKING; Edge et al. 2013). The KiDS and VIKING surveys were designed to be complementary and combine optical and near-infrared imaging in nine photometric bands (Wright et al. 2020). We analyze the now public weak lensing shear catalogue dubbed KiDS-1000 from Giblin et al. (2021), which images 1006 deg^2 on the sky [2]. This data set is divided in four photometric redshift bins of width $\Delta z = 0.2$ in the range $0.1 \leq z_B \leq 0.9$ and a fifth bin with $0.9 \leq z_B \leq 1.2$, based on their most probable Bayesian redshift z_B inferred with the code BPZ (Benítez 2000). The redshift distributions of the five tomographic bins are then calibrated with deep spectroscopic samples that are reweighted using a self-organising map (Wright et al. 2020; Hildebrandt et al. 2021).

As summary statistic of the cosmic shear signal we adopt band power spectra estimated from the two-point correlation functions, which are analysed in Asgari et al. (2021). The corresponding KiDS-1000 cosmic shear likelihood is publicly available in the KiDS Cosmology Analysis Pipeline[3] (KCAP) together with a MontePython interface[4] that wraps the KCAP functionality. This likelihood requires two additional astrophysical nuisance parameters: the amplitude of intrinsic galaxy alignments A_{IA} and the baryonic feedback parameter A_{bary}; see Joachimi et al. (2021) for further details. Furthermore, five additional nuisance parameters δ_z allow for a shift of the mean of the redshift distribution in each tomographic bin within informative Gaussian prior set by the calibration procedure. Since these nuisance parameters do not have a cosmological interpretation we only keep one instance that is shared between the *geometry* and the *growth* instances of the cosmological code.

3.2. Galaxy clustering

The main data source we employ to draw constraints from the BAO and RSD observables are the Sloan Digital Sky Survey III (SDSS III; Eisenstein et al. 2011; Alam et al. 2017) and the Six-Degree Field Galaxy Survey (6dFGS) (Jones et al. 2009; Beutler et al. 2011). Concerning the first of the two surveys, we make use of the twelfth data release of the galaxy clustering data set

---

[2] http://kids.strw.leidenuniv.nl/DR4/lensing.php
[3] https://github.com/KiDS-WL/kcap
[4] https://github.com/BStoelzner/KiDS-1000_MontePython_likelihood

Table 2. Data sets used in our analysis, and their properties.

Probe	Data set	Redshifts	Observable(s)	Data Points
Weak lensing	KiDS-1000 (Kuijken et al. 2019; Hildebrandt et al. 2021; Giblin et al. 2021)	0.1 - 1.2 (photometric redshift)	Tomographic band power spectra $C^{ij}_{\mathrm{E},l}$ (see Eq. 4)	120
Clustering - BAO	BOSS DR12 (Alam et al. 2017)	0.38 - 0.61	$[H(z)]_{\mathrm{fid}}/(\alpha_{\parallel})$; $\alpha_{\perp}[\chi(z)]_{\mathrm{fid}}$ (see Eq. 13)	6
	6dfGS (Jones et al. 2009)	0.106	$r_{\mathrm{s}}(z_{\mathrm{d}})/D_{\mathrm{v}}$	1
Clustering - RSD	BOSS DR12 (Alam et al. 2017)	0.38 - 0.61	$f\sigma_8$	3
Lyα - BAO	eBOSS DR14 (de Sainte Agathe et al. 2019; Blomqvist et al. 2019)	2.34	$\alpha_{\parallel}$; $\alpha_{\perp}$	6360
CMB - BAO	*Planck* 2018 TT, TE, EE + Lowl + lowE (Planck Collaboration et al. 2020a)	~ 1100	$\frac{r_{\mathrm{s}}(z^*)}{D_{\mathrm{A}}(z^*)}$	1
CMB - Primordial	*Planck* 2018 TT, TE, EE + Lowl + lowE (Planck Collaboration et al. 2020a)	~ 1100	$A_{\mathrm{s}}, n_{\mathrm{s}}$	2

Notes. We list the probe, the type of data selected, the redshift range of the probe, the choice of observable, and the size of the data vector. Expressions for the observables are provided in Sect. 2.2. A detailed description of the different data sets can be found in Sect. 3.

of the Baryon Oscillation Spectroscopic Survey (BOSS DR12) which forms part of SDSS III. BOSS DR12 contains records of 1.2 million galaxies over an area of 9329 deg^2 and volume of 18.7 Gpc^3, divided into three partially overlapping redshift slices centred at effective redshifts 0.38, 0.51, and 0.61.

We fit the geometrical relations $\alpha_{\parallel}$ and $\alpha_{\perp}$ (Eq. 8) as reported by the BOSS DR12 data products:

$$\frac{[H(z)]_{\mathrm{fid}}}{\alpha_{\parallel}} = \frac{H(z)[r_{\mathrm{s}}(z_{\mathrm{d}})]_{\mathrm{fid}}}{r_{\mathrm{s}}(z_{\mathrm{d}})}; \quad \alpha_{\perp}[\chi(z)]_{\mathrm{fid}} = \frac{\chi/r_{\mathrm{s}}(z_{\mathrm{d}})}{[r_{\mathrm{s}}(z_{\mathrm{d}})]_{\mathrm{fid}}}, \quad (13)$$

from the reconstruction of the BAO feature at the three different redshift bins where $[r_{\mathrm{s}}(z_{\mathrm{d}})]_{\mathrm{fid}} = 147.78$ Mpc is the scale of the sound horizon at drag epoch as given by the fiducial cosmology used for the reconstruction. $[H(z)]_{\mathrm{fid}}$ and $[\chi(z)]_{\mathrm{fid}}$ are the corresponding Hubble parameter and comoving radial distance for the fiducial cosmology, respectively. Note that when fitting these distance relationships, r_{s} was treated as a free quantity to be determined by the fitting process while r'_{s} was fixed to the value provided in the data products. Moreover, we fit the three redshift measurements of $f\sigma_8(z)$ from RSD obtained using the anisotropic clustering of the pre-reconstruction density field (Alam et al. 2017). The BAO and RSD measurements of BOSS DR12 are two features extracted from the same set of observations. As such, they are not statistically independent. Thus, when analyzing these two features, a combined analysis was performed mediated by the combined covariance matrix of the two sets of measurements from Alam et al. (2017). Moreover, we also account for the correlations present between the three BAO measurements with each other and between the three RSD measurements with each other resulting from the overlap in the used redshift bins.

This treatment of BOSS DR12 data given is different from Tröster et al. (2020b) and Heymans et al. (2021), who perform a combined studies of KiDS with BOSS DR12 in a full-shape analysis. While performing a full-shape analysis in our study would increase the constraining power, it makes discerning between *geometry* and *growth* significantly more complex. Thus, we decided to trade constraining power for clarity in our proposed classification.

The 6dFGS is a combined redshift and peculiar velocity survey covering nearly the entire southern sky. The median redshift of the survey is z = 0.052. The 6dFGS BAO detection offers a constraint on the distance-redshift relation $r_{\mathrm{s}}(z_{\mathrm{d}})/D_{\mathrm{v}}(z_{\mathrm{eff}})$ at $z_{\mathrm{eff}} = 0.106$. Altogether, we employ a total of 10 data points from clustering surveys.

Both the SDSS and the 6dFGS overlap with KiDS in its Northern and Southern patches, respectively. While in principle this induces correlations with the weak lensing measurements, these are comfortably negligible, primarily because of the large survey areas outside the KiDS footprint used for clustering. Moreover, the inferred statistics from the clustering signals tend to originate from larger physical scales than the weak lensing information. Joachimi et al. (2021) showed that cross-correlations between BOSS and KiDS are negligible even for a full-shape clustering analysis, and for the 6dFGS, which is at very low redshift, the correlation is even weaker.

3.3. Lyman-α forest and quasars

We employ high-redshift constraints on the BAO signature from SDSS-IV (Dawson et al. 2016) Data Release 14, observed as part of the extended Baryon Oscillation Spectroscopic Survey (eBOSS; Blanton et al. 2017). We do so by combining the auto- and cross-correlation analyses of three quasar samples from DR14Q (de Sainte Agathe et al. 2019; Blomqvist et al. 2019) which includes quasar clustering and Lyα forest absorption in the Lyα and Lyβ regions. The selected sample of tracer quasars contains 266,590 quasars in the range $1.77 < z_{\mathrm{q}} < 3.5$. It includes 13,406 SDSS DR7 quasars Schneider et al. (2010) and 18,418 broad absorption line (BAL) quasars (Weymann et al. 1991).

The Lyα sample is derived from a super set consisting of 194,166 quasars in the redshift range $2.05 < z_{\mathrm{q}} < 3.5$, whereas the Ly$\beta$ sample is taken from a super set containing 76,650 quasars with $2.55 < z_{\mathrm{q}} < 3.5$.

The BAO signal is detected both parallel and perpendicular to the line of sight in all cases. This allows for the measurement of the distance relationships $\alpha_{\parallel}$ and $\alpha_{\perp}$ described in Eq. (8),

where the fiducial factors of normalization are $[D_M/r_s(z_d)]_{\text{fid}} = 39.26$ and $[D_H/r_s(z_d)]_{\text{fid}} = 8.581$. However, we do not fit the distance relationships directly. Instead, we interpolate the publicly available MCMC chains of the combined analysis of Lyα auto-correlation, quasar auto-correlation and Lyα-quasar cross-correlation[5] from de Sainte Agathe et al. (2019); Blomqvist et al. (2019) and evaluate the 2D interpolation function at the sampled $\alpha_\parallel$ and $\alpha_\perp$ to obtain the corresponding $\Delta\chi^2$-value relative to the best-fit χ^2-value; χ^2_{min}, obtained from Blomqvist et al. (2019, table 5). When reporting the goodness of fit obtained using this likelihood, we employ the following formula $\chi^2 = \Delta\chi^2 + \chi^2_{\text{min}} = \Delta\chi^2 + 6499.31$; where $\Delta\chi^2$ is the value inferred with our likelihood code. When combining this data sets, since goodness of fit values are additive, we simply add $\chi^2_{\text{min}} = 6499.31$ to the obtained $\Delta\chi^2$ of the combined data sets.

3.4. Cosmic microwave background anisotropies

We make use of the constraints resulting from the analysis of measurements of the cosmic microwave background (CMB) temperature and polarization anisotropy maps of the European Space Agency's satellite *Planck* (Planck Collaboration et al. 2020a) denoted as TT, TE, EE + Lowl + lowE and referred to in the following as "Planck 2018". More specifically, we employ the posteriors on the cosmological parameters A_s and n_s as two pseudo data points. Additionally, we adopt *Planck*'s posterior for the BAO angular scale $\theta^* = \frac{D_A(z^*)}{r_{s*}}$, where $z^* \sim 1100$ is the redshift of the end of the recombination epoch.

In order to convert the previously mentioned posteriors into pseudo data points, we employ the PYTHON Monte Carlo sample analysis package GETDIST (Lewis 2019) to first marginalise the public posterior chains of the *Planck* 2018 TT, TE, EE + Lowl + lowE set over all parameters except θ^*, A_s and n_s. Then, we extract the best-fit values of the parameters by finding the maximum of the joint posterior probability density distribution function. Finally, we calculate the combined covariance matrix of the three parameters. In doing so, we approximate the marginalised posterior as a multivariate Gaussian, which is an accurate assumption (see e.g. Fig. A.3). This allows us to associate an error bar with each data point and to evaluate the level of correlation between the three pseudo-measurements. This results in three values that we can match with our theoretical predictions. To distinguish this subset from the complete *Planck* posterior we label it as Recomb This methodology is analogous to that used by Muir et al. (2021) when extracting constraints from a MULTI-NEST chain of the TT + lowl *Planck* lite 2015 likelihood and to the θ^* fitting process in Ruiz & Huterer (2015) .

4. Likelihood analysis

Bayesian inference is employed to obtain constraints for the ΛCDM parameter sets governing the *geometry* and *growth* theory regimes; p^{geom} and p^{grow} respectively. It relies on Bayes' theorem to relate the probability of a given set of parameter values conditioned on the observed data D, known as the posterior probability $P(p_{\text{grow}}, p_{\text{geom}}|D)$, to the probability of observing the data given a set of parameter values, known as the likelihood

$\mathcal{L}(D|p_{\text{grow}}, p_{\text{geom}})$:

$$P(p_{\text{grow}}, p_{\text{geom}}|D) = \frac{\mathcal{L}(D|p_{\text{grow}}, p_{\text{geom}})\Pi(p_{\text{grow}})\Pi(p_{\text{geom}})}{\mathcal{Z}(D)} . \quad (14)$$

Here, we also defined the prior Π for a set of model parameters and the evidence $\mathcal{Z}(D)$, which is independent of the parameters.

In line with previous analyses, we choose a Gaussian likelihood for all data sets under consideration,

$$\mathcal{L}(D|p_{\text{grow}}, p_{\text{geom}})$$
$$= \frac{\exp\{-\frac{1}{2}[D - m(p_{\text{grow}}, p_{\text{geom}})]^T C^{-1}[D - m(p_{\text{grow}}, p_{\text{geom}})]\}}{(2\pi)^{\frac{N}{2}} \sqrt{\det(C)}} . \quad (15)$$

In this general expression, N is the dimension of the data vector, C is covariance matrix that describes the statistical uncertainty and the correlations between the elements of D, and $m(p_{\text{geom}}, p_{\text{grow}})$ is the vector composed of the model predictions for the observations measured in D, given the parameters. This distance is χ^2-distributed for Gaussian data and will be used by us as a measure of the goodness of fit.

Bayesian inference takes into consideration the initial expectations for the values of the parameters prior to analysing the data via $\Pi(p)$. The priors chosen in this work for the parameters in both sets p^{geom} and p^{grow} are the same as in the original KiDS-1000 analysis (Joachimi et al. 2021), which were shown to bare no effect on the S_8 posteriors. We display the prior distributions in Table 3. We note that the KiDS cosmology priors are sufficiently conservative so as not to impact significantly on the posteriors of any of the probe combinations that we consider in this work. The table also provides a brief description of each parameter and specifies their role as either cosmological, nuisance or derived, i.e fully determined from the set of sampling parameters. We also show the treatment of each parameter as either split; i.e. present in both the *geometry* and the *growth* set of parameters, or shared; i.e. a single parameter was used to model both theory regimes.

The *geometry* and *growth* parametrisation entails a duplication of the cosmological parameter space and the associated prior volume, which affects model comparison and selection criteria (Handley & Lemos 2019b). We note that alternative choices of priors could prove useful in this regard. For instance, instead of the sets p^{geom} and p^{grow} one could employ their mean and difference as the sampling parameters. While the mean would be assigned the same set of priors as the traditional analysis, the prior on the parameter differences could more explicitly account for our expectations in deviations from ΛCDM. We will consider these options in future work.

The implementation of Bayesian inference relies on computer methods that make handling the typically high dimensionality of the parameter space feasible. This is especially true in this work where large parts of the parameter space have been doubled. In this work we made use of the cosmological parameter estimation code MONTEPYTHON 2COSMOS[6] (Köhlinger et al. 2019), a modification of MONTEPYTHON (Audren et al. 2013; Brinckmann & Lesgourgues 2019) that allows us to sample duplicated instances of parameters simultaneously. MONTEPYTHON 2COSMOS achieves this by creating two separate instances of its underlying cosmological prediction code, CLASS (Blas et al. 2011; Lesgourgues 2011). Six pre-existing

---

[5] `https://github.com/brinckmann/montepython_public/blob/3.4/data/eBOSS_DR14_scans/eBOSS_DR14_Lya_combined_scan.dat`

[6] `https://github.com/fkoehlin/montepython_2cosmos_public`

Table 3. Model parameters and their priors, adopted from Asgari et al. (2021).

Parameter	Type	Prior	Duplicated	Description
ω_{cdm}	Cosmological	$[0.051, 0.255]$	✓	Reduced cold dark matter density parameter
S_8	Cosmological	$[0.1, 1.3]$	✓	$S_8 = \sigma_8 \sqrt{\frac{\Omega_m}{0.3}}$
ω_b	Cosmological	$[0.019, 0.026]$	✓	Reduced baryonic matter density parameter
n_s	Cosmological	$[0.84, 1.1]$	✓	Spectral index of the primordial curvature power spectrum
h	Cosmological	$[0.64, 0.82]$	✓	Reduced Hubble parameter at present cosmic time
Ω_m	Derived	-	✓	Total matter density parameter
σ_8	Derived	-	✓	Present-time amplitude of matter density fluctuations
A_{IA}	Nuisance	$[-6.0, 6.0]$	✗	Amplitude of intrinsic galaxy alignments
A_{bary}	Nuisance	$[2, 3.13]$	✗	The baryonic feedback on the matter power spectrum
δ_z	Nuisance	$\mathcal{N}(\mu, C)$	✗	Shift of the mean of the KiDS redshift distributions
Ω_k	Fixed	0	✗	Curvature density parameter
$\sum M_{ncdm}$	Fixed	$0.06 \text{ eV}/c^2$	✗	Total mass of massive neutrino species

Notes. The three sections correspond to cosmological, nuisance, and fixed parameters, respectively. The first column provides parameter names, with a brief description given in the fifth column. The second column lists whether parameters are sampled (distinguishing further between cosmological and nuisance parameters), fixed, or determined as a derived parameter from the posterior chain. The third column contains the fiducial parameter value (if fixed) or else the prior range, with the interval indicating the boundaries of a top-hat prior. The five shift parameters δ_z are correlated through their covariance matrix C and their means μ are set to the mean values of the shifts of the tomographic redshift distributions from Hildebrandt et al. (2021). The fourth column shows whether a parameter is duplicated in the geometry–growth split or shared between the two regimes.

likelihoods from MontePython were adapted into MontePython 2COSMOS such that p^{grow} and p^{geom} can be assigned to the models of the observables discussed in Section 2.2; see Fig. 1 for a schematic overview. We employ the nested sampling algorithm MultiNest (Feroz et al. 2009, 2019) which allows us to reliably explore the high-dimensional posterior.

We assume that the likelihoods for the different data sets employed are independent so that they can be combined by simple multiplication, $\mathcal{L}_{tot} = \prod_i^N \mathcal{L}_i$, where N is the number of probes used. The overlap region of the KiDS-1000 and BOSS footprints only accounts for 3% of the BOSS area, and hence it is safe to assume the two data sets are independent, as previous works have shown (Joachimi et al. 2021). Similarly, the BOSS and eBOSS data sets that we employ have been reported to be effectively independent (Ata et al. 2018). Also, the 6dfGS survey has been extensively used as an independent complement to SDSS data, as shown in Beutler et al. (2011).

The constraints of *Planck* 2018 are known to be in tension with those of KiDS-1000 in ΛCDM and therefore should not be combined per se. This tension has also been shown to persist even when the A_s value is fixed; see Tröster et al. (2020a). However, the tension does not manifest in the subset of parameter constraints that we adopt from *Planck* (see Fig. A.3 for reference). While the *Planck* pseudo data points are independent of the low-redshift probes, joint posteriors employing this information will be necessarily correlated with full *Planck* constraints that we display alongside.

5. Results

In this section we present constraints on the *geometry* and *growth* cosmological parameters combining the weak lensing, clustering, Lyman-α, and Recomb data sets. In Appendix A, we verify that these data sets are fully consistent with each other, and that our 'traditional' re-analysis of each data sets is consistent with the analyses presented in the literature. We also analyse the goodness of fit for each data combination finding that in all studied cases the models offer a good fit of the data. Moreover, we compare the traditional and *geometry-growth* split analysis, find-
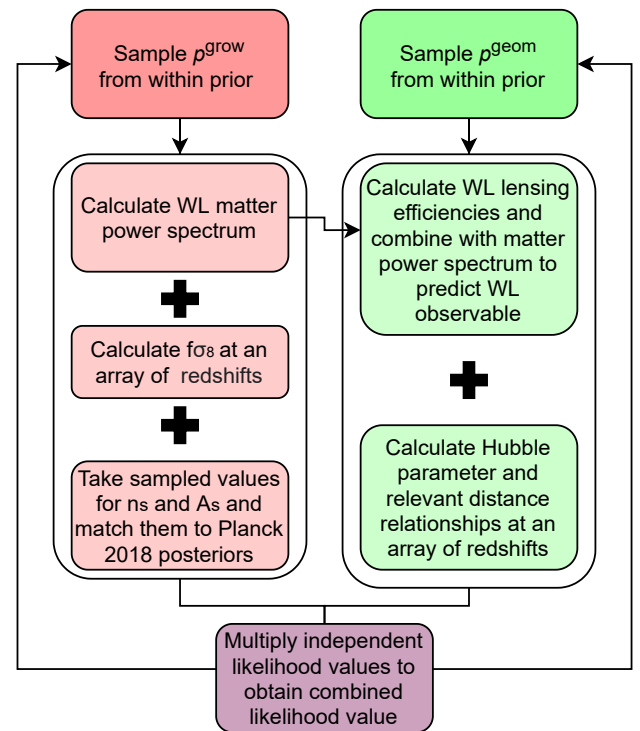

Fig. 1. Schematic of the complete MontePython 2COSMOS pipeline developed for the purposes of this work. Two instances of the cosmological code, cosmology 1 and cosmology 2, independently sample the cosmological parameters for the two theory regimes, *geometry* and *growth*, respectively. These parameters are then passed to the likelihood modules to calculate the theoretical prediction for each individual probe. Finally, the respective independent likelihood values for each probe are multiplied to obtain the likelihood value of the combined data set.

ing that while the split model is better at fitting the data, the improvement is not decisive at justifying the extra added degrees of freedom with respect the traditional analysis; see Appendix B for further details.

5.1. Geometry versus growth constraints

The marginalised posterior distributions for a subset of cosmological parameters, namely Ω_m, σ_8, and h, are illustrated in Fig. 2 for the split analysis of *geometry* (grey) and *growth* (green) as well as the traditional analysis with one single set of cosmological parameters (red). The leftmost row corresponds to an analysis of weak lensing data alone, while the rows to the right show the results obtained by subsequently adding the clustering, Lyman-α, and Recomb data sets. Additionally, we display the constraints from the *Planck* 2018 analysis (Planck Collaboration et al. 2020a) for reference in each panel (blue). The corresponding marginalised 1D posteriors are shown in Fig. C.1 and the posteriors of the full set of cosmological parameters are presented in Appendix D.

We find that the constraining power on the *geometry* and *growth* theory regimes differs depending on the sensitivity of the probes with respect to the various cosmological parameter in the two theory regimes. For the parameters Ω_m or ω_{cdm} the constraining power of *geometry* and *growth* is comparable. Potential discrepancies in these parameters would thus be the most meaningful as both regimes are informed by the data. We also observe cosmological parameters for which only one theory regime has a significant constraining power. This is the case for S_8, n_s and σ_8, which are only constrained by the *growth* regime. Consequently, the posteriors of their *geometry* counterparts are driven by the prior. Conversely, we find that h is overwhelmingly dominated by the *geometry* regime while its *growth* posterior remains unconstrained by the data. It is important to stress that while it is possible for the *geometry* regime to be uninformed about the perturbatory cosmological parameters, the *growth* theory regime necessarily holds information, even if very limited, on the background parameters since the perturbatory aspects of the theory are built from this background cosmology. Finally, we note that ω_b is poorly constrained in both regimes with the data sets used.

The *geometry* and *growth* regimes explore independent directions of the parameter space, which results in posterior distributions of Ω_m and σ_8 that are orthogonal to each other. Figure 2 shows that this orthogonality significantly strengthens as more data sets are combined. A lack of correlation between $\boldsymbol{p}^{geom}$ and $\boldsymbol{p}^{grow}$ supports the meaningfulness of the *geometry* and *growth* categories as distinct theory regimes. The constraints on Ω_m from *growth* and on σ_8 from *geometry* are mainly dominated by the prior, except for the combination of weak lensing + clustering + Lyman-α + Recomb data, which puts stronger constraints from the *growth* regime on Ω_m. This causes the two regimes to span over two independent directions in parameter space. While Ω_m^{grow} is largely unconstrained, it is consistent with Ω_m^{geom} for all probe combinations, as detailed in Fig. 3. This finding deviates somewhat from the similar study by Muir et al. (2021) who found a 2σ preference for higher values of Ω_m^{grow} than Ω_m^{geom} in their combined probe analysis.

Positive correlation can be interpreted as a sign of consistency between *geometry* and *growth* as it indicates that when one instance of the parameter is varied, its counterpart mimics its change. Thus, the two theory aspects portray the same trend. Conversely, negative correlation would be a sign of lack of consistency in the *geometry* and *growth* split. Overall, we observe minimal or little correlation between the different pairs of cosmological parameters for any of the studied combinations of data sets, finding all pairs of cosmological parameter to have a correlation coefficient below 0.2. The exception to this rule is the Ω_m pair for which we observe a positive correlation of 0.48 between Ω_m^{geom} - Ω_m^{grow} when solely analysing weak lensing data, which is sensitive to both theory regimes. The correlation vanishes once additional data sources are included as these put stronger constraints on Ω_m^{geo} while leaving Ω_m^{gro} mostly unchanged.

The bottom row of Fig. 2 shows the marginalised posterior distributions for Ω_m and h. The weak lensing observable by itself is not sensitive to the Hubble parameter, which is why the posterior distributions for h are prior-dominated for both *geometry* and *growth*, as well as for the traditional analysis. By adding additional data sets to the analysis, the *geometry* constraints shrink while the *growth* ones remain significantly wider, narrowing towards a $\Omega_m h = $ const degeneracy constrained by the peak position of the matter power spectrum.

Comparing the posterior resulting from the traditional analysis to the ones obtained in the split analysis of the two theory regimes in the top row of Fig. 2, we find that, as was expected, the traditional contours reside at the intersection between the *geometry* and *growth* contours. While the constraints on Ω_m and σ_8 from *geometry* and *growth* by themselves are quite weak, the combination of the two regimes results in the "banana-shaped" contour, which is most noticeable in the leftmost panel showing the constraints obtained from solely analysing weak lensing data. The good agreement between the two theory regimes internally and the traditional constraints is also evidenced by the negligible change in the goodness of fit; see Table B.1. However, tension with the full *Planck* analysis remains throughout, which we will discuss further in Section 5.2.

We quantify the level of consistency between the two theory regimes by considering the posterior distribution of the difference between the parameter duplicates, which is shown in Fig. 4 for three selected cosmological parameters: S_8, Ω_m, and h. Visually, the marginalised posterior distributions show good agreement with the zero point. This indicates no tension between parameters in the two theory regimes. We quantify the tension between parameter duplicates following the methodology of Köhlinger et al. (2019). We find good agreement between theory regimes for all combinations of parameters with a maximum offset of 1.27σ which is observed in the posterior distribution of Δh and $\Delta \Omega_m$ for weak lensing + clustering data.

Finally, we do not observe any new correlations between the different instances of the cosmological parameters and the nuisance parameters beyond those present in the traditional analysis. In particular, we do not see a correlation between the *growth* instance of Ω_m and the nuisance parameter A_{IA} as reported for weak lensing data by Muir et al. (2021). We also repeated our analysis splitting in addition the parameter A_{IA}. We obtained consistent results with constraints beyond the prior exclusively on the *geometry* instance of A_{IA}. This is reassuring as it indicates that the data constrains intrinsic alignments solely through the different redshift scaling of its contribution relative to weak lensing.

5.2. Tension with full Planck data

The presence of tension between our analyses and the full *Planck* contours suggests that its cause may lie in the weak lensing observable, common to all cases of study, or in the ΛCDM model. The most recent cosmic shear analysis of KiDS-1000 (Asgari et al. 2021) found a 3σ disagreement in their estimate of the cosmological parameter S_8 with respect to the prediction of the *Planck* 2018 analysis of the CMB. This tension has been shown to persist both when combining the KiDS-1000 data with other probes (Heymans et al. 2021) and when considering extensions of the ΛCDM model (Tröster et al. 2020a).
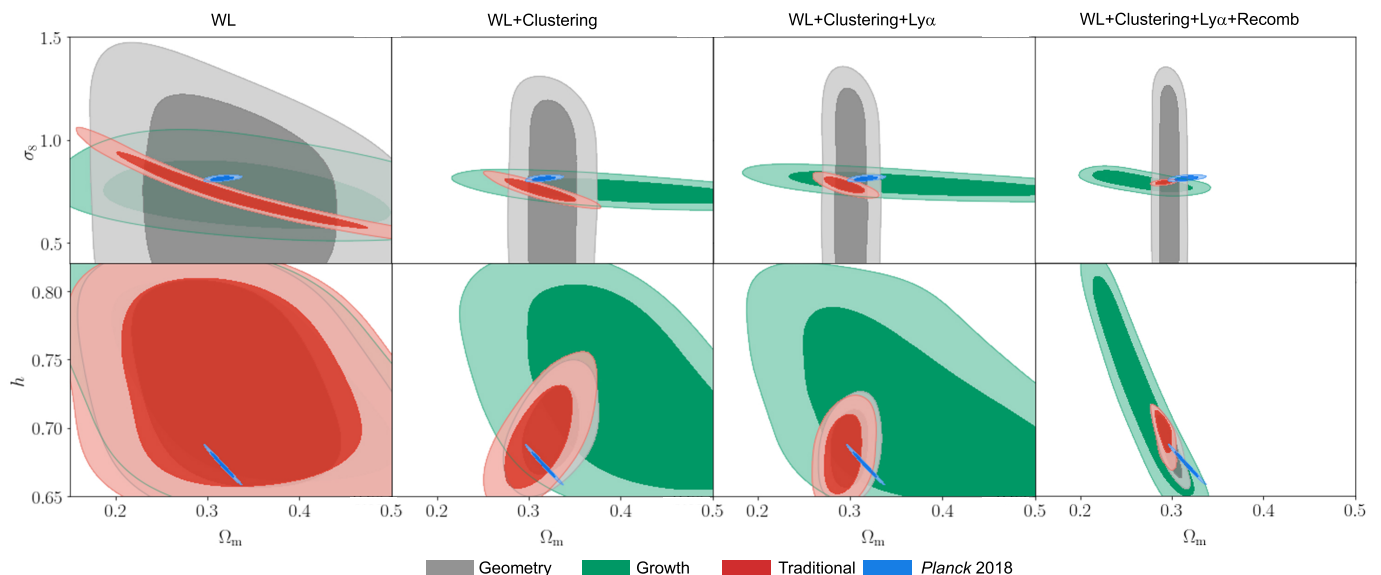
Fig. 2. Marginalised posterior distributions of σ_8 and Ω_m (top row), as well as h and Ω_m (bottom row) for different combinations of data sets (columns). Each panel shows a superposition of four contours. Namely, the *growth* and *geometry* contours from the split analysis of the two theory regimes (green and grey contours respectively), the contour resulting from the traditional analysis with one set of cosmological parameters (red), and the reference contours from the *Planck* 2018 analysis (blue; Planck Collaboration et al. 2020a).
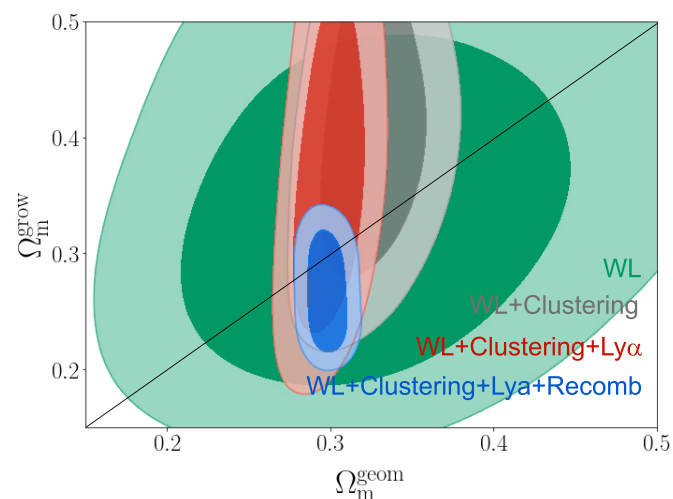
Fig. 3. Marginalised posterior for Ω_m when comparing their *geometry* (horizontal axis) and *growth* (vertical axis) counterparts. We show the evolution of the contours as more data sources are added into the analysis. Namely, we display weak lensing (green), weak lensing combined with clustering data (grey), weak lensing combined with clustering and Lyman-α forest data (red) and finally weak lensing combined with clustering, Lyman-α forest and Recomb data (blue).

Fig. 4. Marginalised posterior distributions of the difference between *geometry* and *growth* parameter duplicates of S_8, Ω_m, and h. Each panel shows the contours for the combinations of data sets WL (green), WL + Clustering (black), WL + Clustering + Lyα (red) and WL + Clustering + Lyα + Recomb (blue). At the top-left corner of each panel we display the σ-level tension of each contour with respect to the null value $p^{\mathrm{grow}} = p^{\mathrm{geom}}$ for all combination of data sets.

The level of consistency between BOSS DR12 data on galaxy clustering (Alam et al. 2017) and *Planck* 2018 depends on the chosen parametrisation (Sánchez et al. 2017; Loureiro et al. 2019; Kobayashi et al. 2020). Tröster et al. (2020b) showed that when employing the geometrical quantities $\alpha_\perp$ and $\alpha_\parallel$ the data is not in tension with the ΛCDM parameters of *Planck* 2018. When cast into ΛCDM, the full shape analysis BOSS DR12 prefers a lower value of σ_8 than *Planck* 2018 at 2.1σ. However, when the tension is computed for the whole parameter space, the two probes are in good agreement. The same considerations have to be made when assessing the consistency of the eBOSS DR14

data set with other surveys. In the $\alpha_\perp$ and $\alpha_\parallel$ framework, the eBOSS DR14 has been shown to be consistent with the *Planck* 2016 (Planck Collaboration et al. 2016a) best-fit flat ΛCDM model, with a mild deviation of 1.7σ (Blomqvist et al. 2019). However, a non-negligible degree of discrepancy has been reported when constraints are cast into the ΛCDM framework, es-
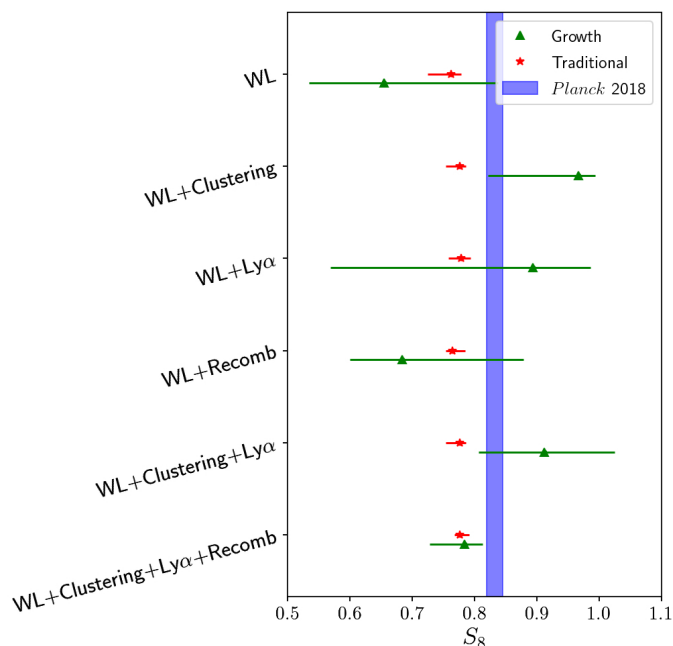
Fig. 5. The figure shows the S_8 best-fit parameter values with their associated 1σ confidence regions obtained from the different combinations of data sets explored in this work. In top to bottom order we display the data sets WL, WL + Clustering, WL + Lyα, WL + Recomb, WL + Clustering + Lyα and finally WL + Clustering + Lyα + Recomb The numerical value of the quantities displayed can be found in Tab. 4.

pecially in the Hubble parameter (Aubourg et al. 2015; Addison et al. 2018).

Finally, our implementation of the CMB data directly uses *Planck* 2018 posteriors as pseudo data points ensuring a perfect agreement with the early-Universe probe. Thus, of the four data sets considered in this work, only KiDS-1000 is in significant tension with *Planck* 2018. This is simply a consequence of the tension manifesting in the amplitude of structure growth for which the weak lensing data are most constraining. Nonetheless, this does not exclude the possibility of new tensions appearing upon the combination of data sets which independently are in good agreement with *Planck* 2018; see e.g. the discussion for Ω_m and h below.

Since we use KiDS-1000 as our base observable in all combinations of data sets, we observe that the tension on S_8 carries on to all our combinations of data sets. While the tension can already be appreciated in Figs. 2 and C.1, we highlight this disagreement in Fig. 5, which shows the constraints on the parameter S_8 for all the studied combinations of data sets, and for the traditional and *growth* parameters (the *geometry* constraints default to the prior and are not shown). We also show the maximum posterior (MAP) values for S_8 and the associated 68% credible interval (CI) calculated using its projected joint highest posterior density PJ-HPD (see Joachimi et al. 2021 for reference) in Table 4. The MAP values are directly inferred from the posterior distribution of sampling parameters. However, the limited number of samples in the posterior chains leads to some scatter in the MAP values, which is noticeable for the broader posterior in the weak lensing-only case. Therefore, we infer the MAP values for this specific data set using the Nelder-Mead optimisation method (Nelder & Mead 1965; see Joachimi et al. 2021 for details).

We explicitly quantify this tension under the assumption of Gaussian and independent marginal posteriors. In this case the tension τ between two data sets i and j for a parameter p is given

by

$$\tau_{ij} = \frac{|\overline{p}_i - \overline{p}_j|}{\sqrt{\mathrm{Var}[p_i] + \mathrm{Var}[p_j]}} \;, \tag{16}$$

where the barred quantities refer to the mean values of the distributions and Var to their variance. We provide the obtained τ values in Table 5. We see that the tension between the traditional and *Planck* 2018 S_8 posterior distributions stays within 2 to 3σ for all combinations of data sets. The *growth* constraints are much weaker and hence not in tension although the combined constraint prefers a lower S_8 value than *Planck*. We observe a slightly lower tension in S_8 between KiDS-1000 only and *Planck* 2018 than Asgari et al. (2021) who employed a different summary statistic (COSEBIs) for their tension assessment. It is important to note that no particular choice of summary statistics is more powerful or more discrepant. Instead, the variance in the reported tension value for each summary statistics is due to slight differences in the degeneracy direction between the statistics which the parameter S_8 does not perfectly capture. Moreover, our mean estimate is obtained directly from the posterior chains sampled with MultiNest, which is less accurate than the Nelder-Mead optimisation of Asgari et al. (2021).

It is remarkable that the level of tension increases by 0.3σ when our Recomb data, i.e. the acoustic peak angular scale and the primordial power spectrum parameters, is included in the analysis. From Table 4, it is possible to see Clustering and Lyman-α data push the S_8 constraints towards higher values more affine to the full *Planck* result, whereas Recomb; a subset of the CMB data, has the opposite effect, which may seem counter-intuitive. However, we argue that this trend can be understood as a manifestation of the high versus low multipole discrepancy within *Planck*; see Fig. 21 of Planck Collaboration et al. (2020a). The parameters we have employed in our analysis are largely informed by multipoles $\ell < 800$, and the low-ℓ *Planck* posterior is in excellent agreement with our joint probe analysis.

In contrast, the tentative signs of tension with the full *Planck* constraints manifest not only in S_8 or σ_8, but extend to Ω_m and h; as seen in Fig. 2. Discrepancy levels for Ω_m are also given in Table 5 and reach 2.8σ for the joint probe analysis including Recomb data and 2.4σ in the WL + Clustering + Lyα + Recomb case. The Lyman-α forest data also has a preference for a somewhat lower Ω_m than full *Planck*, which translates into a 2.3σ discrepancy. While the non-Gaussian shape of the marginal posterior for h prevents us from applying Eq. (16) more generally, in the WL + Clustering + Lyα + Recomb case the contours are sufficiently close to normal to apply the tension estimator, yielding a 2.0σ tension in h. In agreement with the low-ℓ *Planck* posterior, our joint probe posterior prefers lower values of Ω_m and higher values of h than full *Planck*, with MAP values of $\Omega_m \approx 0.289^{+0.007}_{-0.005}$ and $h \approx 0.705^{+0.007}_{-0.015}$.

It is important to bear in mind that our joint probe analysis including the Recomb data is not statistically independent from the full *Planck* 2018 constraints, violating the assumption made to obtain Eq. (16). We leave a quantification of the level of correlation to future work. In principle, this correlation could lower or increase tension, dependent on the parameter degeneracies in the complement of the *Planck* data that we did not employ in our analysis. However, since the *Planck* high-ℓ constraints display the same degeneracy directions for the key parameters Ω_m, σ_8, and h as the low-ℓ subset, it is reasonable to assume that this correlation is positive, and hence our tension estimates of Table 4 are lower bounds on the true level of discrepancy.

Table 4. Marginal S_8 constraints.

Data set	MAP + PJ-HPD			Marginal		
	S_8^{trad}	S_8^{geom}	S_8^{grow}	S_8^{trad}	S_8^{geom}	S_8^{grow}
WL	$0.762^{+0.016}_{-0.037}$	$0.704^{+0.402}_{-0.300}$	$0.654^{+0.183}_{-0.120}$	0.751 ± 0.027	0.719 ± 0.310	0.779 ± 0.139
WL + Clustering	$0.776^{+0.010}_{-0.022}$	$0.676^{+0.610}_{-0.184}$	$0.966^{+0.027}_{-0.145}$	0.768 ± 0.016	0.700 ± 0.326	0.871 ± 0.077
WL + Lyα	$0.778^{+0.015}_{-0.021}$	$0.373^{+0.639}_{-0.116}$	$0.893^{+0.324}_{-0.324}$	0.772 ± 0.017	0.700 ± 0.326	0.902 ± 0.160
WL + Recomb	$0.764^{+0.021}_{-0.011}$	$0.762^{+0.505}_{-0.282}$	$0.684^{+0.191}_{-0.084}$	0.768 ± 0.016	0.701 ± 0.328	0.828 ± 0.131
WL + Clustering + Lyα	$0.777^{+0.009}_{-0.023}$	$0.375^{+0.627}_{-0.140}$	$0.911^{+0.114}_{-0.105}$	0.769 ± 0.016	0.695 ± 0.328	0.867 ± 0.091
WL + Clustering + Lyα + Recomb	$0.776^{+0.016}_{-0.008}$	$0.468^{+0.533}_{-0.261}$	$0.783^{+0.029}_{-0.056}$	0.781 ± 0.012	0.702 ± 0.336	0.748 ± 0.035

Notes. The first three columns display the maximum posterior (MAP) values for S_8 and its 68% credible interval (CI) calculated using its projected joint highest posterior density (PJ-HPD). The last three columns display the obtained marginal constraints on S_8 in the form of mean ± standard deviation calculated using `GetDist`. In both sets of constraints the first column displays the traditional constraints, the middle column the constraints found by the *geometry* regime and last column those of the *growth* regime.

Table 5. Level of tension for the parameters S_8 and Ω_{m}.

Tension with *Planck*	S_8	Ω_{m}
WL	2.62	0.19
WL + Clustering	2.65	0.11
WL + Lyα	2.64	2.28
WL + Recomb	2.65*	2.82*
WL + Clustering + Lyα	2.65	1.43
WL + Clustering + Lyα + Recomb	2.91*	2.40*

Notes. Tension was calculated using the method of difference of Gaussians between the traditional constraints and those of *Planck* 2018 (Planck Collaboration et al. 2020a). The entries marked by a star employ a subset of *Planck* CMB data in the probe combination and are therefore not statistically independent.

6. Conclusions

In this work we developed a multi-probe self-consistency test of the spatially flat ΛCDM model with the aim of exploring potential causes of the cosmic tension within the current cosmological theory. In order to do so, we divided our model into two theory regimes, *geometry* and *growth*, distinguishing between the strictly homogeneous and isotropic background and the formation of matter density fluctuations on top of this background, respectively. Making use of this distinction, we classified a series of cosmological observables, or parts thereof, as *geometry* or *growth* depending on the theory regime needed to model them within the ΛCDM model. We duplicated the ΛCDM parameter space into two independent copies, $\boldsymbol{p}^{\text{grow}}$ and $\boldsymbol{p}^{\text{geom}}$, and let each govern its respective set of observables.

As cosmological observables, we employed weak lensing (WL) cosmic shear measurements from the latest data release of the Kilo Degree Survey (KiDS-1000), and measurements of the galaxy and Lyman-α (Lyα) BAO feature distance relationship from the 12th data release of the Baryon Oscillation Spectroscopic Survey (BOSS DR12), as well as from the 14th data release of the extended Baryon Oscillation Spectroscopic Survey (eBOSS DR14) and the 6 Degree Field Galaxy Survey (6dFGS). We also used growth rate measurements from BOSS DR12. Moreover, we made use of the *Planck* 2018 posterior distributions for the cosmological parameters A_{s} and n_{s} and the angular scale of the sound horizon θ^* as pseudo-data points. We

grouped these observables into four data sets: WL comprised of the KiDS-1000 data, Clustering which combined BOSS DR12 and the 6dfGS galaxy clustering measurements, Lyα composed of eBOSS DR14 data, and Recomb containing the subset of the *Planck* 2018 posterior. Constraints for $\boldsymbol{p}^{\text{grow}}$ and $\boldsymbol{p}^{\text{geom}}$ were obtained using a modified version of the Bayesian parameter estimation code MONTEPYTHON 2COSMOS. In order to explore the extended parameter space we made use of Monte Carlo Markov chains while employing the nested sampler MULTINEST. The code developed to perform this analysis is made publicly available [7].

We generally found very good agreement between all probes considered, including the subset of CMB data we used, with little variation in the goodness of fit. The *geometry* and *growth* parameters are consistent throughout, and the additional degrees of freedom in the model due to the split are not preferred by the data. The constraints on $\boldsymbol{p}^{\text{grow}}$ and $\boldsymbol{p}^{\text{geom}}$ converge towards the those found by the traditional ΛCDM analysis that does not duplicate parameters for all the studied combinations of data sets. We also observed that $\boldsymbol{p}^{\text{grow}}$ and $\boldsymbol{p}^{\text{geom}}$ explore different directions of the parameter space, their contours tending to be orthogonal to each other. Thus, we conclude that our constraints on $\boldsymbol{p}^{\text{grow}}$ and $\boldsymbol{p}^{\text{geom}}$ support the *geometry* vs *growth* distinction as a meaningful classification of the ΛCDM model.

Regarding the S_8 parameter tension between low- and high-redshift probes, our analysis produced tension levels between 2 and 3σ for the traditional constraints of different probe combinations and *Planck* 2018 (Planck Collaboration et al. 2020a). The joint probe *growth* constraint on S_8 also prefers lower values, but is not in tension due to substantially larger statistical errors. The parameters Ω_{m} and h also reach discrepancies in the 2 and 3σ range, with larger values preferred for h and smaller values preferred for Ω_{m}, in particular when our subset of CMB data is included. As the latter is primarily informed by large angular scales in the Recomb, this result supports earlier indications that the cosmic tensions in S_8, and possibly also H_0, are driven by multipoles $\ell > 800$ in *Planck* (Addison et al. 2016; Planck Collaboration et al. 2020a).

In comparison to the recent similar analysis by Muir et al. (2021), our work employs an alternative distinction between *geometry* and *growth* solely based on the need to consider mat-

---

[7] `https://github.com/BStoelzner/KiDS_geometry_vs_growth`

ter anisotropies in the modelling of the cosmological observable, irrespective of whether the matter anisotropies reside in the present or early Universe. This leads to a different classification of cosmological observables between the two works. Nonetheless, both Muir et al. (2021) and this work report an excellent degree of agreement between the two considered regimes. However, we do not observe the slight preference for higher values of $\Omega_{\mathrm{m}}^{\mathrm{grow}}$ as seen by Muir et al. (2021), nor do we find any significant correlations between $\Omega_{\mathrm{m}}^{\mathrm{grow}}$ and the shared nuisance parameter for the intrinsic alignment amplitude, A_{IA}.

To conclude we outline possible avenues for improvements that future iterations of the methodology presented in this work could consider. On the theoretical side, it would be interesting to study the feasibility of *geometry* vs *growth* splits beyond ΛCDM. It is clear that the distinction proposed in this work can be extrapolated straightforwardly to modified models that only introduce changes to the background cosmology, such as non-flat ΛCDM models or dark energy models with an effective equation of state, which have proven to be successful at encapsulating a wide variety of models (Traykova et al. 2021; García-García et al. 2020). Another type of modification that is compatible with this framework is an effective Newton's constant for gravity because it does not change the shape of the Jeans equation (Baker et al. 2014). Other, more involved modifications could include scale-dependent modifications to the growth of structure. More general parametrisations than a simple duplication of ΛCDM parameters would have to be considered, and the link between the background and the growth of structure, via the Jeans equation and its non-linear corrections, carefully investigated.

Future applications should strive to incorporate new measurements on similar or different physical observables that could be added as new sources of constraining power. Specially, efforts should be directed towards performing a full-shape analysis of the LSS matter power spectrum as shown in Tröster et al. (2020b) and Heymans et al. (2021) instead of the BAO and RSD feature analysis used in this work. Similarly, the current treatment of CMB data should be replaced by a more rigorous *geometry* and *growth* analysis of the full CMB dataset, complemented by an analogous split of the CMB lensing likelihood (Planck Collaboration et al. 2020b) observable equivalent to the one undertaken for KiDS-1000.

In addition to this, we recommend updating the galaxy clustering data to the latest eBOSS DR16 release (Alam et al. 2021) which also includes σ_8 at high redshifts from quasar density measurements as well as high-redshift galaxy measurements (Zhao et al. 2021). Particularly adding to the currently weaker *growth* constraints, future works could consider studying the addition of Sunyaev-Zeldovich measurements of cluster counts (Planck Collaboration et al. 2016b), as well as the Integrated Sachs-Wolfe effect (Planck Collaboration et al. 2016c; Stölzner et al. 2018). The *geometry* vs *growth* approach holds promise to yield novel insights with the powerful data from forthcoming surveys, including DESI [8] (DESI Collaboration et al. 2016), Euclid [9] (Laureijs et al. 2011), and the LSST at the Rubin Observatory [10] (The LSST Dark Energy Science Collaboration et al. 2018).

---

[8] https://www.desi.lbl.gov/
[9] https://www.euclid-ec.org/
[10] https://www.lsst.org/

ticipation Group, Universidad Nacional Autónoma de México, University of Arizona, University of Colorado Boulder, University of Oxford, University of Portsmouth, University of Utah, University of Virginia, University of Washington, University of Wisconsin, Vanderbilt University, and Yale University.

References

Abate, A. & Lahav, O. 2008, MNRAS, 389, L47
Abbott, T. M. C., Abdalla, F. B., Alarcon, A., et al. 2018a, Phys. Rev. D, 98, 043526
Abbott, T. M. C., Abdalla, F. B., Alarcon, A., et al. 2018b, Phys. Rev. D, 98, 043526
Abellan, G. F., Murgia, R., Poulin, V., & Lavalle, J. 2020, arXiv e-prints, arXiv:2008.09615
Addison, G. E., Huang, Y., Watts, D. J., et al. 2016, ApJ, 818, 132
Addison, G. E., Watts, D. J., Bennett, C. L., et al. 2018, ApJ, 853, 119
Alam, S., Ata, M., Bailey, S., et al. 2017, MNRAS, 470, 2617
Alam, S., Aubert, M., Avila, S., et al. 2021, Phys. Rev. D, 103, 083533
Alam, U., Sahni, V., & Starobinsky, A. A. 2009, ApJ, 704, 1086
Alcock, C. & Paczynski, B. 1979, Nature, 281, 358
Alsing, J., Heavens, A., & Jaffe, A. H. 2017, MNRAS, 466, 3272
Andrae, R., Schulze-Hartung, T., & Melchior, P. 2010, arXiv e-prints, arXiv:1012.3754
Asgari, M., Lin, C.-A., Joachimi, B., et al. 2021, A&A, 645, A104
Ata, M., Baumgarten, F., Bautista, J., et al. 2018, MNRAS, 473, 4773
Aubourg, É., Bailey, S., Bautista, J. E., et al. 2015, Phys. Rev. D, 92, 123516
Audren, B., Lesgourgues, J., Benabed, K., & Prunet, S. 2013, JCAP, 1302, 001
Baker, T., Ferreira, P., & Skordis, C. 2014, Phys. Rev. D, 89, 024026
Bartelmann, M. & Schneider, P. 2001, Phys. Rep., 340, 291
Benítez, N. 2000, ApJ, 536, 571
Bernal, J. L., Verde, L., & Cuesta, A. J. 2016, J. Cosmology Astropart. Phys., 2016, 059
Beutler, F., Blake, C., Colless, M., et al. 2011, MNRAS, 416, 3017
Beutler, F., Seo, H.-J., Saito, S., et al. 2017, MNRAS, 466, 2242
BeyondPlanck Collaboration, Andersen, K. J., Aurlien, R., et al. 2020, arXiv e-prints, arXiv:2011.05609
Blanton, M. R., Bershady, M. A., Abolfathi, B., et al. 2017, AJ, 154, 28
Blas, D., Lesgourgues, J., & Tram, T. 2011, J. Cosmology Astropart. Phys., 2011, 034
Blomqvist, M., du Mas des Bourboux, H., Busca, N. G., et al. 2019, A&A, 629, A86
Brinckmann, T. & Lesgourgues, J. 2019, Physics of the Dark Universe, 24, 100260
Capistrano, A. J. S., Cabral, L. A., Marão, J. A. P. F., & Coimbra-Araújo, C. H. 2020, arXiv e-prints, arXiv:2009.02167
Chu, M. & Knox, L. 2005, ApJ, 620, 1
Clarkson, C., Ellis, G., Larena, J., & Umeh, O. 2011, arXiv e-prints, arXiv:1109.2314
Condon, J. J. & Matthews, A. M. 2018, PASP, 130, 073001
Cuceu, A., Farr, J., Lemos, P., & Font-Ribera, A. 2019, J. Cosmology Astropart. Phys., 2019, 044
Dawson, K. S., Kneib, J.-P., Percival, W. J., et al. 2016, AJ, 151, 44
de Sainte Agathe, V., Balland, C., du Mas des Bourboux, H., et al. 2019, A&A, 629, A85
DESI Collaboration, Aghamousa, A., Aguilar, J., et al. 2016, arXiv e-prints, arXiv:1611.00036
Doux, C., Baxter, E., Lemos, P., et al. 2021, MNRAS, 503, 2688
du Mas des Bourboux, H., Rich, J., Font-Ribera, A., et al. 2020, ApJ, 901, 153
Edge, A., Sutherland, W., Kuijken, K., et al. 2013, The Messenger, 154, 32
Efstathiou, G. & Bond, J. R. 1999, MNRAS, 304, 75
Efstathiou, G. & Gratton, S. 2019, arXiv e-prints, arXiv:1910.00483
Eisenstein, D. J., Weinberg, D. H., Agol, E., et al. 2011, AJ, 142, 72
Feroz, F., Hobson, M. P., & Bridges, M. 2009, MNRAS, 398, 1601
Feroz, F., Hobson, M. P., Cameron, E., & Pettitt, A. N. 2019, The Open Journal of Astrophysics, 2, 10
Freedman, W. L., Madore, B. F., Hatt, D., et al. 2019, ApJ, 882, 34
García-García, C., Bellini, E., Ferreira, P. G., Traykova, D., & Zumalacárregui, M. 2020, Phys. Rev. D, 101, 063508
Gelman, A., Carlin, J. B., Stern, H. S., & Rubin, D. B. 2004, Bayesian Data Analysis, 2nd edn. (Chapman and Hall/CRC)

Giblin, B., Heymans, C., Asgari, M., et al. 2021, A&A, 645, A105
Hamilton, A. J. S. 1998, Linear Redshift Distortions: a Review, Vol. 231 (in "The Evolving Universe" ed. D. Hamilton, Kluwer Academic, p. 185-275 (1998)), 185
Handley, W. & Lemos, P. 2019a, Phys. Rev. D, 100, 023512
Handley, W. & Lemos, P. 2019b, Phys. Rev. D, 100, 043504
Harris, C. R., Millman, K. J., van der Walt, S. J., et al. 2020, Nature, 585, 357
Heymans, C., Tröster, T., Asgari, M., et al. 2021, A&A, 646, A140
Hildebrandt, H., Köhlinger, F., van den Busch, J. L., et al. 2020, A&A, 633, A69
Hildebrandt, H., van den Busch, J. L., Wright, A. H., et al. 2021, A&A, 647, A124
Hu, W. & Dodelson, S. 2002, ARA&A, 40, 171
Joachimi, B., Lin, C. A., Asgari, M., et al. 2021, A&A, 646, A129
Jones, D. H., Read, M. A., Saunders, W., et al. 2009, MNRAS, 399, 683
Joudaki, S., Blake, C., Heymans, C., et al. 2017a, MNRAS, 465, 2033
Joudaki, S., Blake, C., Heymans, C., et al. 2017b, MNRAS, 465, 2033
Kaiser, N. 1987, MNRAS, 227, 1
Kass, R. E. & Raftery, A. E. 1995, Journal of the American Statistical Association, 90, 773
Kobayashi, Y., Nishimichi, T., Takada, M., & Takahashi, R. 2020, Phys. Rev. D, 101, 023510
Köhlinger, F., Joachimi, B., Asgari, M., et al. 2019, MNRAS, 484, 3126
Komatsu, E., Dunkley, J., Nolta, M. R., et al. 2009, ApJS, 180, 330
Kosowsky, A., Milosavljevic, M., & Jimenez, R. 2002, Phys. Rev. D, 66, 063007
Kuijken, K., Heymans, C., Dvornik, A., et al. 2019, A&A, 625, A2
Lahav, O. & Liddle, A. R. 2019, arXiv e-prints, arXiv:1912.03687
Laureijs, R., Amiaux, J., Arduini, S., et al. 2011, arXiv e-prints, arXiv:1110.3193
Laurent, P., Eftekharzadeh, S., Le Goff, J.-M., et al. 2017, J. Cosmology Astropart. Phys., 2017, 017
Lemos, P., Raveri, M., Campos, A., et al. 2020, arXiv e-prints, arXiv:2012.09554
Lesgourgues, J. 2011, arXiv e-prints, arXiv:1104.2932
Lewis, A. 2019, arXiv e-prints, arXiv:1910.13970
Limber, D. N. 1953, ApJ, 117, 134
Loureiro, A., Moraes, B., Abdalla, F. B., et al. 2019, MNRAS, 485, 326
Muir, J., Baxter, E., Miranda, V., et al. 2021, Phys. Rev. D, 103, 023528
Mukhanov, V. 2004, International Journal of Theoretical Physics, 43, 623
Mörtsell, E. & Dhawan, S. 2018, 2018 IOP Publishing Ltd and Sissa Medialab Journal of Cosmology and Astroparticle Physics, 2018
Nelder, J. A. & Mead, R. 1965, The Computer Journal, 7, 308
Nesseris, S. & Perivolaropoulos, L. 2007, J. Cosmology Astropart. Phys., 2007, 018
Peebles, P. J. E. & Yu, J. T. 1970, ApJ, 162, 815
Pesce, D. W., Braatz, J. A., Reid, M. J., et al. 2020, ApJ, 891, L1
Planck Collaboration, Ade, P. A. R., Aghanim, N., et al. 2016a, A&A, 594, A13
Planck Collaboration, Ade, P. A. R., Aghanim, N., et al. 2016b, A&A, 594, A24
Planck Collaboration, Ade, P. A. R., Aghanim, N., et al. 2016c, A&A, 594, A21
Planck Collaboration, Aghanim, N., Akrami, Y., et al. 2020a, A&A, 641, A6
Planck Collaboration, Aghanim, N., Akrami, Y., et al. 2020b, A&A, 641, A8
Raveri, M. & Hu, W. 2019, Phys. Rev. D, 99, 043506
Riess, A. G., Casertano, S., Yuan, W., et al. 2021, ApJ, 908, L6
Ruiz, E. J. & Huterer, D. 2015, Phys. Rev. D, 91, 063009
Sánchez, A. G., Scoccimarro, R., Crocce, M., et al. 2017, MNRAS, 464, 1640
Schneider, D. P., Richards, G. T., Hall, P. B., et al. 2010, AJ, 139, 2360
Schneider, P., van Waerbeke, L., Kilbinger, M., & Mellier, Y. 2002, A&A, 396, 1
Silvestri, A., Pogosian, L., & Buniy, R. V. 2013, Phys. Rev. D, 87, 104015
Spiegelhalter, D. J., Best, N. G., Carlin, B. P., & Van Der Linde, A. 2002, Journal of the Royal Statistical Society: Series B (Statistical Methodology), 64, 583
Stölzner, B., Cuoco, A., Lesgourgues, J., & Bilicki, M. 2018, Phys. Rev. D, 97, 063506
The LSST Dark Energy Science Collaboration, Mandelbaum, R., Eifler, T., et al. 2018, arXiv e-prints, arXiv:1809.01669
Traykova, D., Bellini, E., Ferreira, P. G., et al. 2021, arXiv e-prints, arXiv:2103.11195
Tröster, T., Asgari, M., Blake, C., et al. 2020a, arXiv e-prints, arXiv:2010.16416
Tröster, T., Sánchez, A. G., Asgari, M., et al. 2020b, A&A, 633, L10
van den Busch, J. L., Hildebrandt, H., Wright, A. H., et al. 2020, A&A, 642, A200
van Uitert, E., Joachimi, B., Joudaki, S., et al. 2018, MNRAS, 476, 4662
Vargas-Magaña, M., Ho, S., Cuesta, A. J., et al. 2018, MNRAS, 477, 1153
Virtanen, P., Gommers, R., Oliphant, T. E., et al. 2020, Nature Methods, 17, 261
Vonlanthen, M., Räsänen, S., & Durrer, R. 2010, J. Cosmology Astropart. Phys., 2010, 023
Wang, S., Hui, L., May, M., & Haiman, Z. 2007, Phys. Rev. D, 76, 063503
Weymann, R. J., Morris, S. L., Foltz, C. B., & Hewett, P. C. 1991, ApJ, 373, 23
Wright, A. H., Hildebrandt, H., Kuijken, K., et al. 2019, A&A, 632, A34
Wright, A. H., Hildebrandt, H., van den Busch, J. L., & Heymans, C. 2020, A&A, 637, A100
Zhao, G.-B., Wang, Y., Taruya, A., et al. 2021, MNRAS, 504, 33

Appendix A: Consistency of data sets

We present a comparison between the posteriors of a separate analysis of the weak lensing data set and the individual analyses of clustering, Lyman-α, and Recomb data. In Fig. A.1 we compare the individual posteriors for weak lensing (black) and clustering (green) with the constraints from the combined analysis of the two data sets (red). Additionally, we show the *Planck* 2018 contours (Planck Collaboration et al. 2020a) for reference (blue). Similarly, we show a comparison between weak lensing and Lyman-α data in Fig. A.2 and between weak lensing and Recomb data in Fig. A.3. We note that the Recomb data set, shown as green contours in Fig. A.3, is composed of pseudo data points for θ^*, A_s, and n_s which are inferred via marginalisation of the fiducial *Planck* posteriors over the remaining cosmological parameters, as described in Section 3.4.

Our traditional constraints, i.e. with a single set of cosmological parameters governing *geometry* and *growth*, are in excellent agreement with the fiducial analyses of the band power spectra in Asgari et al. (2021), the BOSS DR12 consensus analysis in Alam et al. (2017) and the analysis of eBOSS DR14 data in Cuceu et al. (2019). Moreover, the Recomb data analysis recovers the *Planck* posterior for the parameters n_s, A_s and θ^*, as expected. The n_s and A_s posteriors impose constraints along S_8 or σ_8, which are consistent with *Planck* constraints but significantly broader. Similarly, the θ^* measurement imposes a degenerate constraint in the $h - \omega_{\rm cdm}$ plane which contains the *Planck* 2018 contours; see Fig. A.3 for details. We observe that for the three combinations of KiDS data with external data sets, i.e "K1K+Clustering", "K1K+Lyα" and "K1K+CMB", the posterior contours of the respective combined analysis fall at the intersection of the posteriors of the two individual data sets; see Figs. A.1, A.2, and A.3.

Appendix B: Goodness of fit

In Table B.1 we provide the best-fit χ^2-values, inferred from the maximum of the posterior, for each combination of data sets that we consider, and for both the split analysis of *geometry* and *growth* as well as the traditional analysis. Additionally, we show the number of free parameters employed in each of the analyses ($n_{\rm params}$), as well as the associated number of data points ($n_{\rm points}$). We note that in this work we adopted the fiducial KiDS-1000 cosmology covariance matrix. The fiducial results of Asgari et al. (2021), however, were obtained with an iterated covariance model which is based on the best-fit parameters of Heymans et al. (2021). While the covariance model has a negligible impact on the posteriors (see Asgari et al. 2021), it does impact the numerical χ^2-value inferred from the maximum of the posterior at the few-percent level. Therefore, the best-fit χ^2-values reported in Table B.1 are not directly comparable to the ones reported in Asgari et al. (2021).

It is common practice to assess the goodness of fit under the assumption that the χ^2 statistic follows a χ^2 distribution with the number of degrees of freedom DoF = $n_{\rm points} - n_{\rm params}$. The reduced χ^2, which is defined by $\overline{\chi}^2 = \chi^2/$DoF, is then used as a measure of goodness of fit. However, this assumption requires that the data is normally distributed, that the model is linearly dependent on the sampling parameters, and that there is no informative prior on the parameter ranges (see for instance Joachimi et al. 2021). These conditions do not hold in general in cosmological analyses, which require a more sophisticated estimate of the effective number of degrees of freedom which can be inferred for example from mocks or posterior predictive data realisations

(Andrae et al. 2010; Spiegelhalter et al. 2002; Handley & Lemos 2019a; Raveri & Hu 2019; Joachimi et al. 2021).

For the weak lensing data set used in this work, Joachimi et al. (2021) report an effective number of degrees of freedom of $n_{\rm params,eff} = 4.5$. We cannot simply adopt this number since the split of cosmological parameters into two theory regimes and the addition of external data sets is expected to have an impact on the effective number of degrees of freedom. Therefore, we restrict the analysis to an interpretation of the commonly used approximation of the degrees of freedom as the difference between the number of data points and the number of parameters, which is conservative in identifying underfitting models. Nevertheless, we treat the five nuisance parameters that parameterise a shift in the mean of the five KiDS redshift bins as essentially fixed by their strongly informative Gaussian prior and thus we do not count them as free parameters.

The reduced χ^2 for KiDS weak lensing is fairly high. As discussed in detail in Asgari et al. (2021), this result only occurs for the band power statistic and does not appear to point to a systematically underfitting model. We also applied our split analysis to an earlier KiDS data release (cf. Wright et al. 2019) and found consistent results with good χ^2. The combination with any of the other data sets acts to reduce the reduced χ^2 closer to unity, so that there is no sign of inconsistency between the probes we combine. We observe that the split analyses show a slightly better fit than their traditional counterparts represented by smaller values of χ^2. However, comparing the reduced χ^2, which takes the increased number of model parameters into account, we do not find a significant preference for the split model. Thus, we conclude that while the split model is better at fitting the data, such improvement is not decisive at justifying the extra added degrees of freedom with respect to the traditional analysis.

Moreover, we calculate the Bayes factor (Kass & Raftery 1995),

$$\mathcal{B} = \frac{\mathcal{Z}_{\rm trad}}{\mathcal{Z}_{\rm split}}, \tag{B.1}$$

where $\mathcal{Z}$ is the Bayesian evidence found for each model (see Eq. 14 for reference), as well as the difference between the Deviance Information Criterion (DIC; Gelman et al. 2004),

$$\text{DIC} = \frac{1}{2}\text{Var}[\chi^2] - \overline{\chi^2}, \tag{B.2}$$

between the traditional and split model for each data set. The bar denotes the mean over the sampled χ^2 values. Positive values of $\ln \mathcal{B}$ correspond to larger Bayesian evidence in support of the traditional model; negative values to preference for the split model. Models with a lower DIC are preferred by the data since they either possess a lower mean χ^2; i.e. a better fit of the data, or a lower variance in their χ^2; i.e. a lower effective number of parameters. Thus, the DIC acts as a combined measurement of goodness of fit and model complexity. Therefore, negative values of $\text{DIC}_{\rm trad} - \text{DIC}_{\rm split}$ represent a preference for the traditional model while negative values support the split model.

The obtained values are shown in Table B.2. In order to asses the significance of the values reported by both metrics we follow the criteria laid out in Joudaki et al. (2017b). We interpret $-1 < \ln \mathcal{B} < 1$ and $\text{DIC}_{\rm trad} - \text{DIC}_{\rm split} < 5$ values as not to be significant enough to prefer either of the models. Therefore, we conclude that neither the Bayes factor nor the DIC show a preference for the split or the traditional model.

Table B.1. Best-fit χ^2 values for all different combinations of data sets considered.

	χ^2		DoF		$\overline{\chi}^2$	
Data sets	Trad.	Split	Trad.	Split	Trad.	Split
WL	152.34	150.76	120 - 7	120 - 12	1.35	1.40
WL + Clustering	157.49	156.36	130 - 7	130 - 12	1.28	1.33
WL + Lyα	152.37 + 6499.31	152.82 + 6499.31	6483 - 7	6483 - 12	1.03	1.03
WL + Recomb	151.67	152.75	123 - 7	123 - 12	1.32	1.37
WL + Clustering + Lyα	161.33 + 6499.31	160.76 + 6499.31	6493 - 7	6493 - 12	1.03	1.03
WL + Clustering + Lyα + Recomb	163.16 + 6499.31	161.19 + 6499.31	6496 - 7	6496 - 12	1.03	1.03

Notes. Shown are the best-fit χ^2 values, the corresponding number of degrees of freedom (DoF), and the goodness of fit $\overline{\chi}^2$. Values are given for both the *geometry* and *growth* split analysis and the traditional analysis. Note that in the rows reporting on results from Lyman-α forest data we make the contribution to the joint χ^2 from the eBOSS DR14 baseline explicit; see Section 3.3 for more details.

Table B.2. Model comparison between the traditional and the split model, using the Bayes factor $\mathcal{B}$ and the DIC.

Data set	$\ln \mathcal{B}$	DIC_{trad} - DIC_{split}
WL	0.139	0.855
WL + Clustering	-0.103	1.153
WL + Lyα	0.001	1.104
WL + Recomb	-0.051	1.035
WL + Clustering + Lyα	0.221	1.047
WL + Clustering + Lyα + Recomb	0.630	0.998

Appendix C: Marginalised 1D posterior distributions

In Fig. C.1 we provide the marginalised 1D posteriors for h, Ω_m, and σ_8, corresponding to the posteriors shown in Fig. 2, for the combination of weak lensing, clustering, Lyman-α, and Recomb data sets.

Appendix D: Full cosmological posteriors

In this appendix we present the full set of posterior distributions for all cosmological parameters and for each of the studied combinations of data sets shown in Fig. 2. In Fig. D.1 we show the marginalised posterior in an analysis of weak lensing data, while Figs. D.2, D.3, and D.4 show the constraints in an analysis of weak lensing + clustering, weak lensing + clustering + Lyman-α, and weak lensing + clustering + Lyman-α + Recomb data, respectively. In each figure we provide the constraints on *geometry* and *growth* parameters from a split analysis of the two theory regimes (grey and green contours), as well the traditional analysis with one set of cosmological parameters (red). Additionally, we show the *Planck* 2018 contours (Planck Collaboration et al. 2020a) for reference (blue).
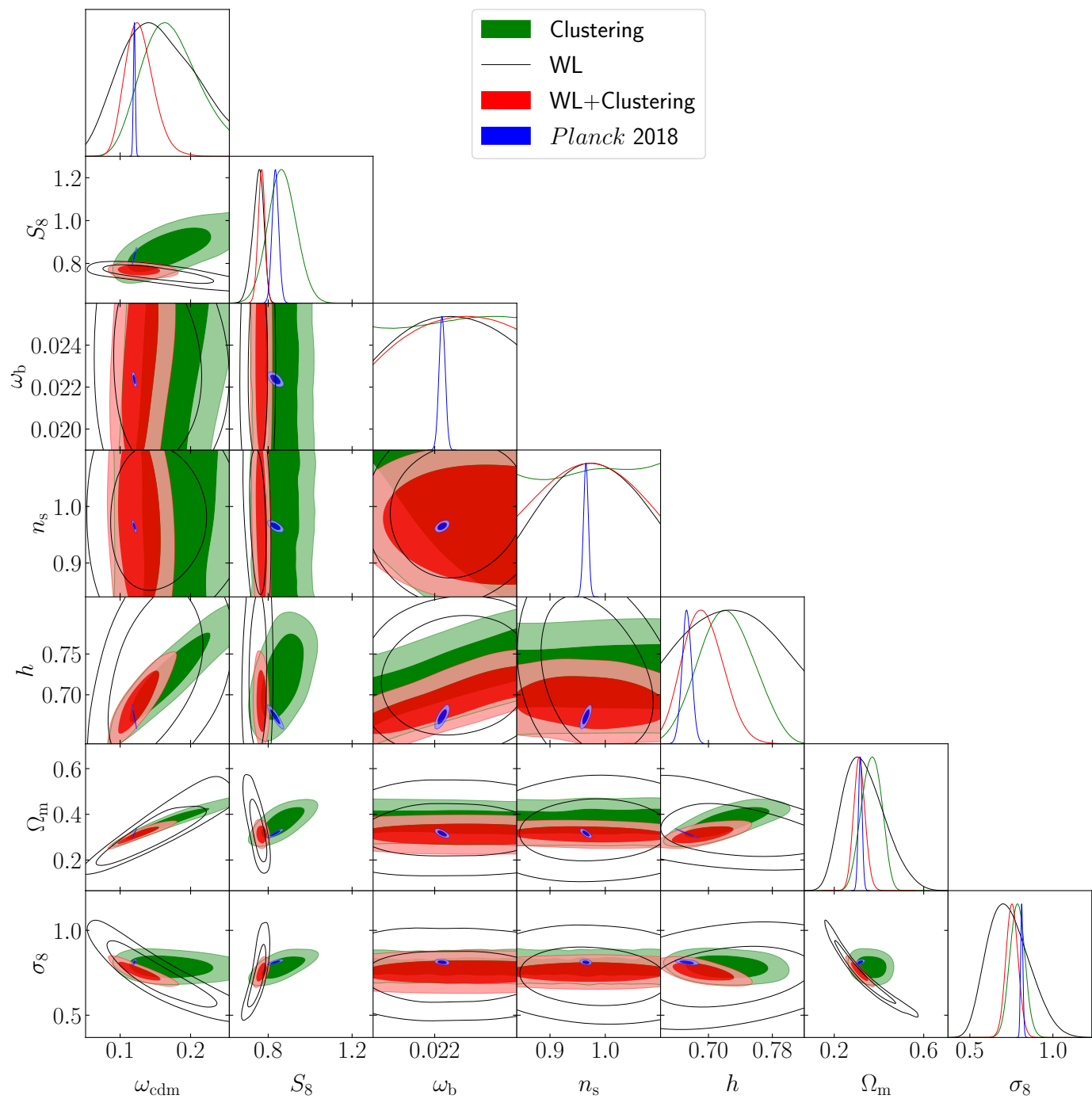
Fig. A.1. Marginalised posteriors distributions from the analysis of the WL and Clustering data sets. Each panel shows the posterior resulting from a separate analysis of clustering (green) and weak lensing (black) data sets as well as the combination of both data sets (red). Additionally, we show the *Planck* 2018 contours (Planck Collaboration et al. 2020a) for reference (blue).
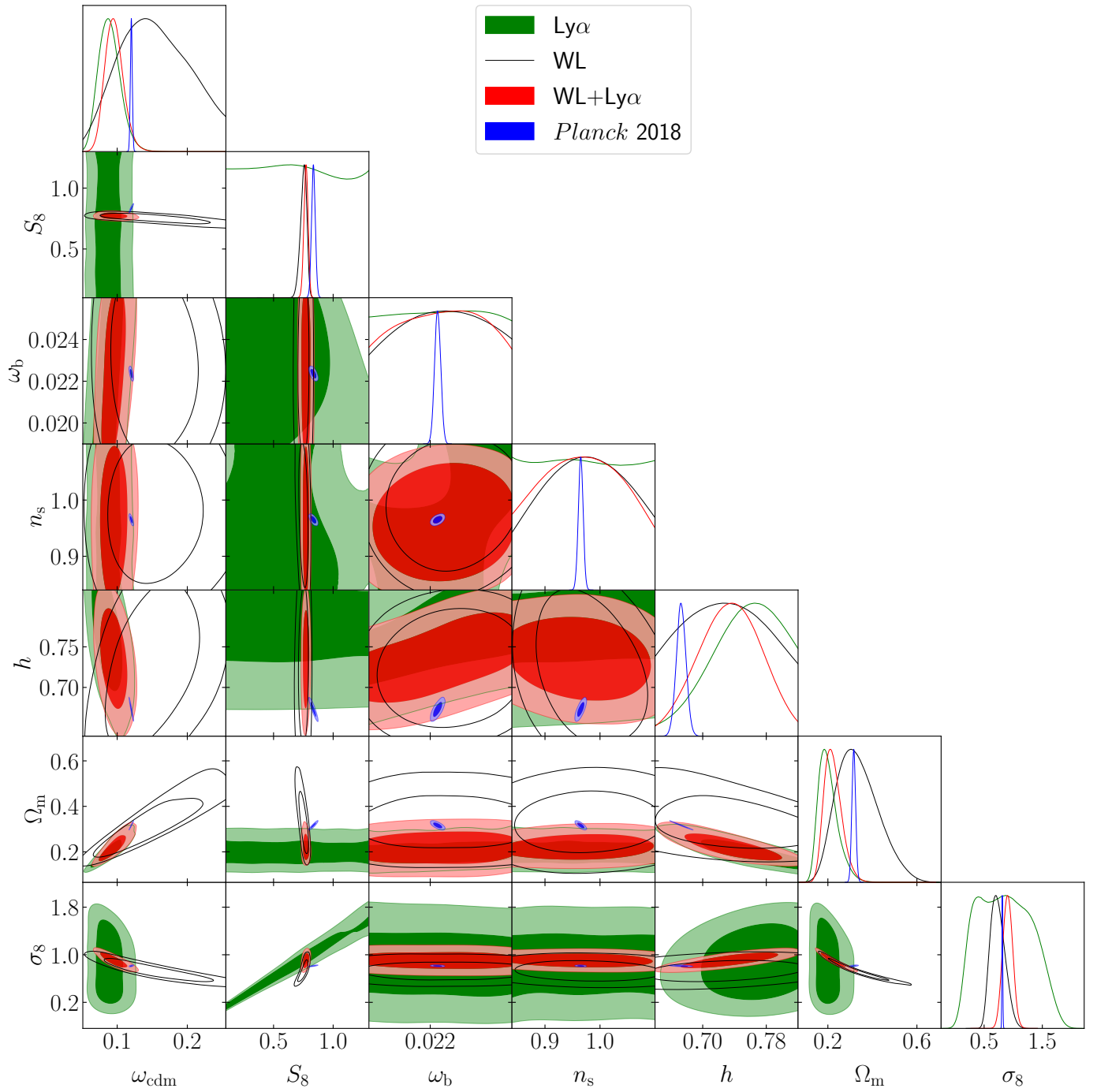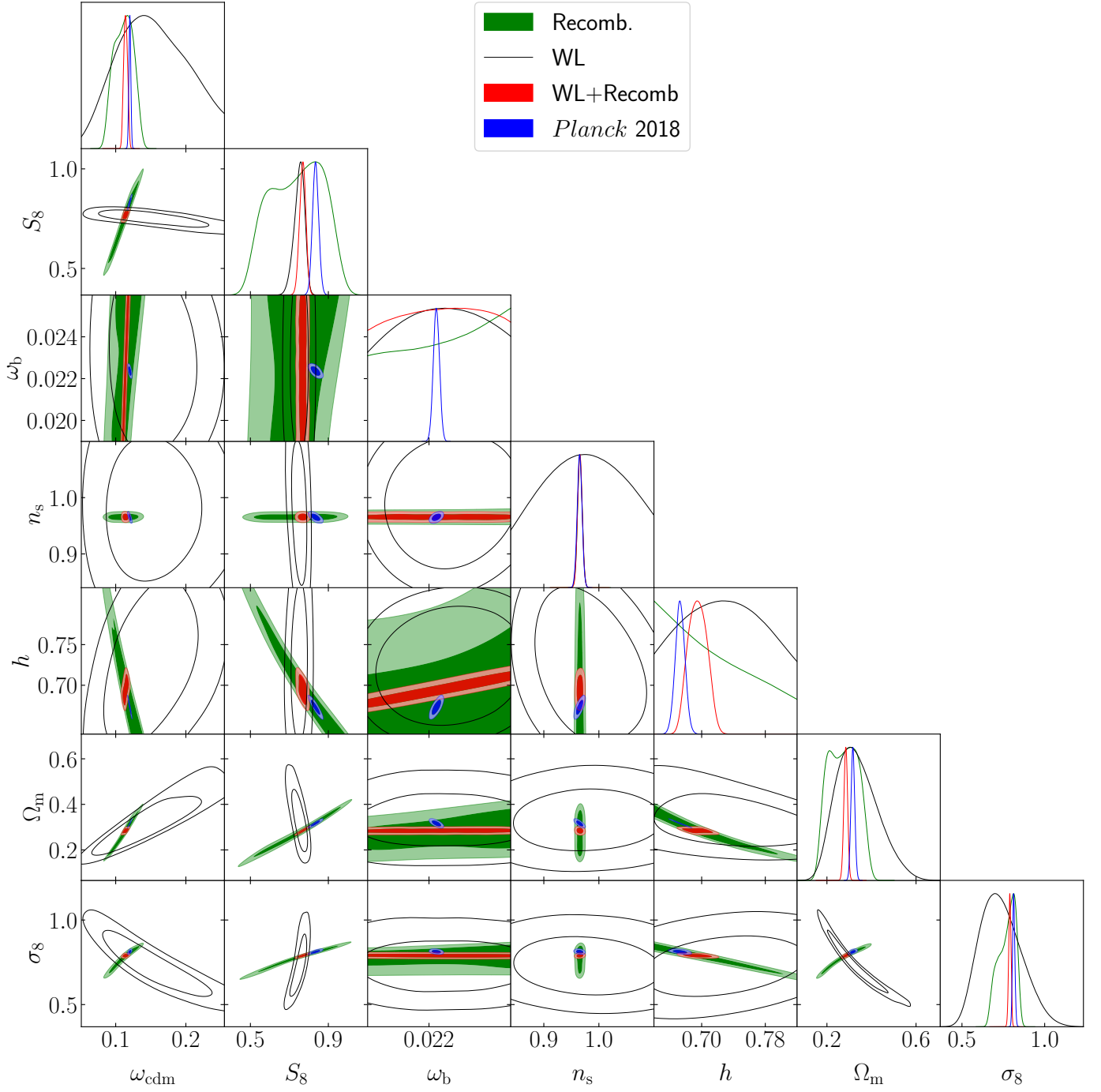
Fig. A.2. Marginalised posteriors distributions from the analysis of the WL and Ly-α data sets. Each panel shows the posterior resulting from a separate analysis of Lyman-α (green) and weak lensing (black) data sets as well as the combination of both data sets (red). Additionally, we show the *Planck* 2018 contours (Planck Collaboration et al. 2020a) for reference (blue).
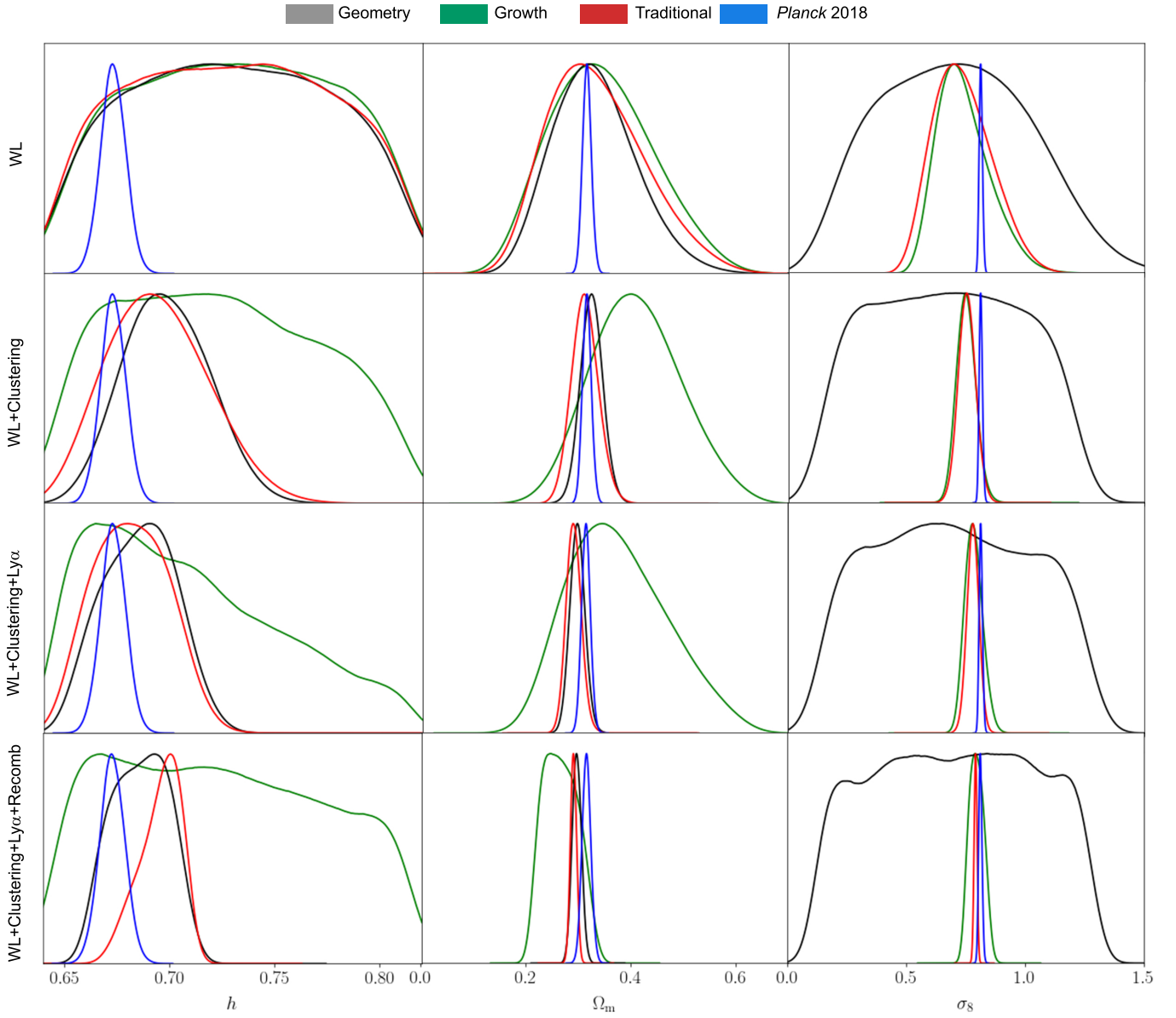
Fig. A.3. Marginalised posteriors distributions from the analysis of the WL and Recomb data sets. The Recomb data set is composed of pseudo data points for θ^*, A_s, and n_s which are inferred via marginalisation of the fiducial *Planck* posteriors (Planck Collaboration et al. 2020a) over the remaining cosmological parameters, as described in Section 3.4. Each panel shows the posterior resulting from a separate analysis of Recomb (green) and weak lensing (black) data sets as well as the combination of both data sets (red). Additionally, we show the *Planck* 2018 contours for reference (blue).

Fig. C.1. Marginalised 1D posterior distributions of the cosmological parameters h (first column), $\Omega_{\rm m}$ (second column) and σ_8 (third column) for different combinations of data sets (rows). The first row shows the constraints from the WL data set only, while the following rows show the constraints obtained when subsequently adding the Clustering, Ly-α, and Recomb data sets. In each panel we show a superposition of the constraints from our split analysis of *growth* and *geometry* theory regimes (green and grey contours respectively), a traditional analysis with one single set of cosmological parameters (red), and the *Planck* 2018 (Planck Collaboration et al. 2020a) constraints for reference (blue).
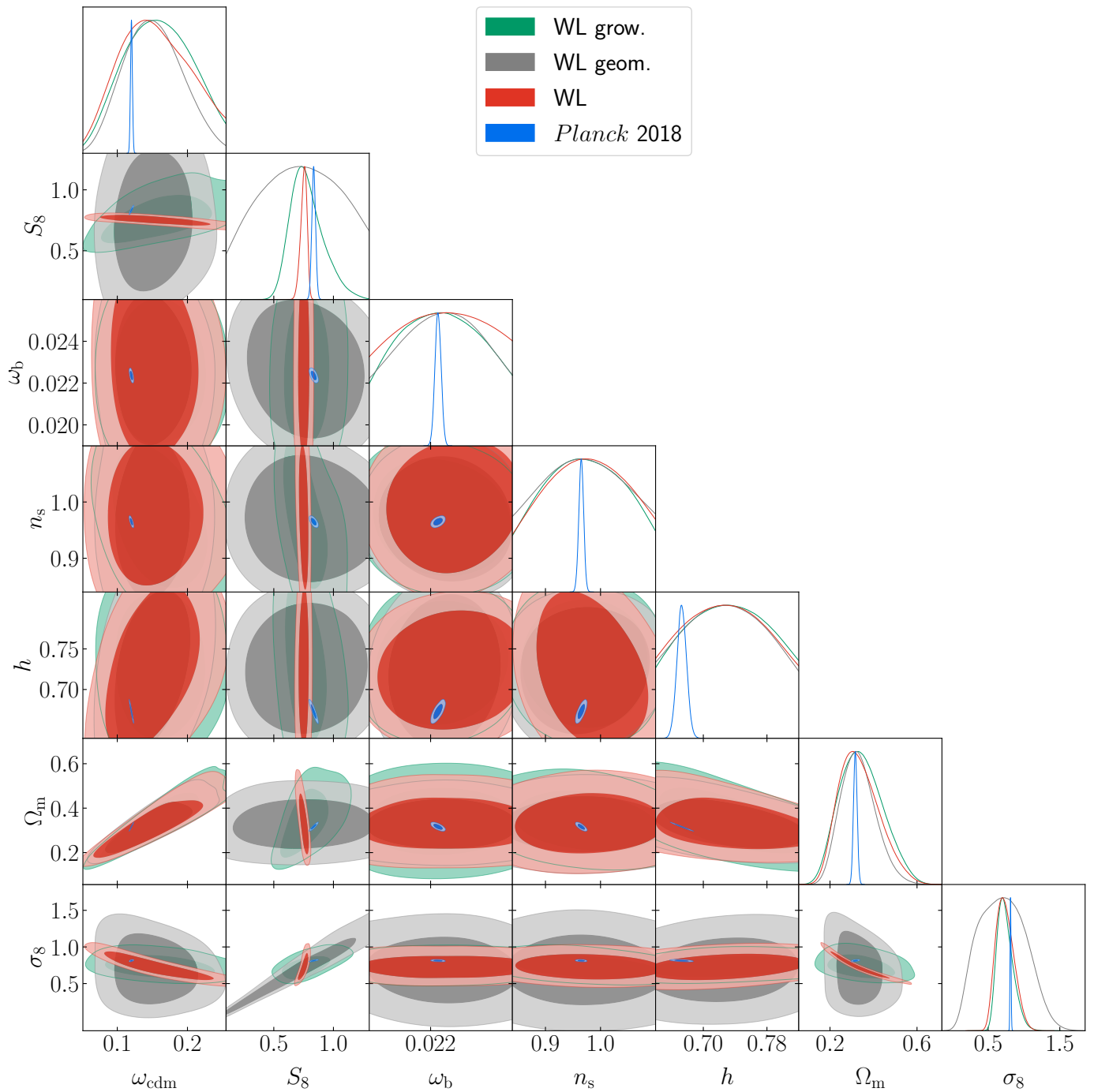
Fig. D.1. Marginalised posteriors from the analysis of the WL data set for all cosmological parameters. Each panel shows a superposition of the *growth* (green), *geometry* (grey), traditional analysis (red), and the *Planck* 2018 contours (Planck Collaboration et al. 2020a) for reference (blue).
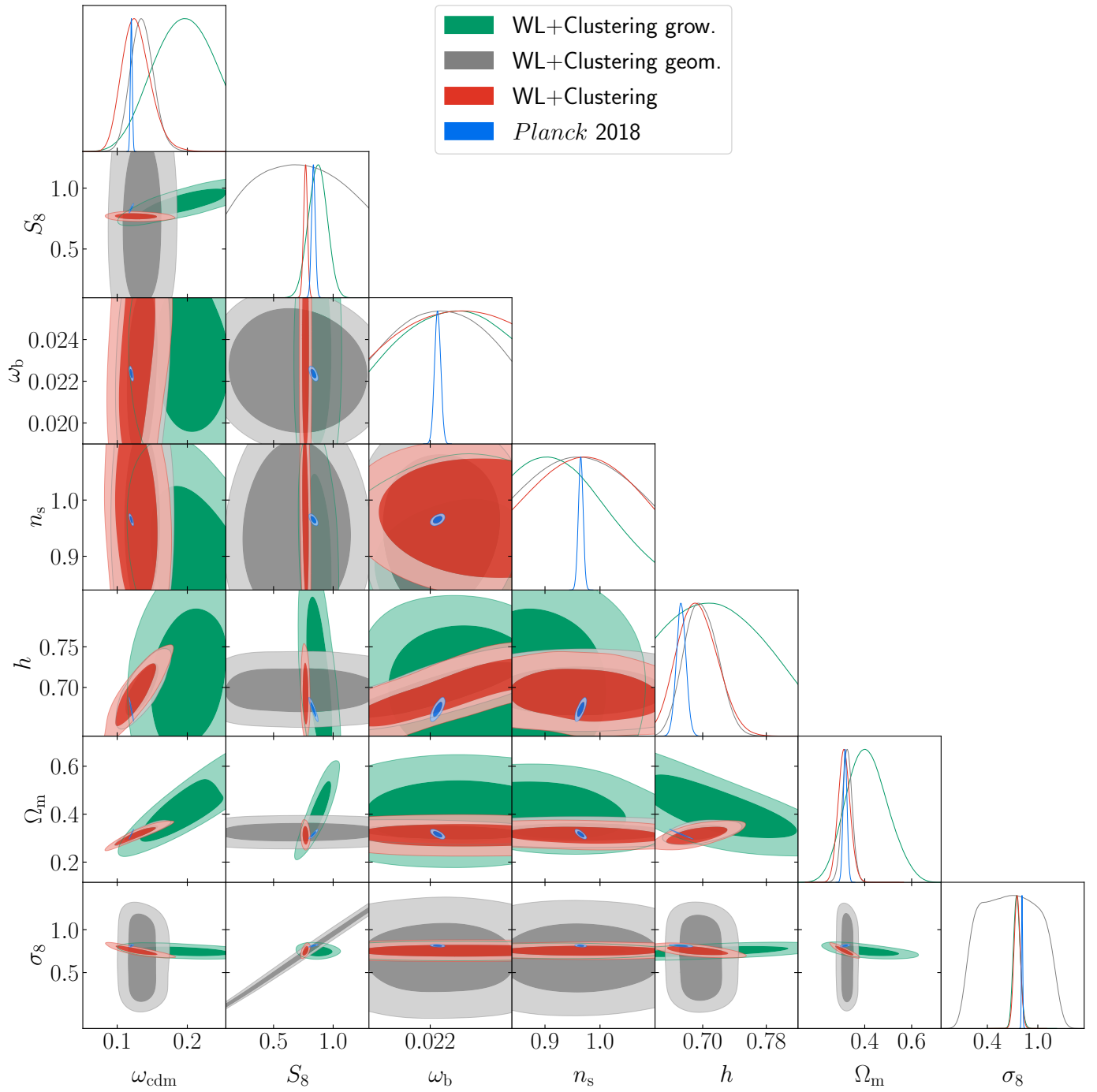
Fig. D.2. Marginalised posteriors from the analysis of the WL + Clustering data sets for all cosmological parameters. Each panel shows a superposition of the *growth* (green), *geometry* (grey), traditional analysis (red), and the *Planck* 2018 contours (Planck Collaboration et al. 2020a) for reference (blue).
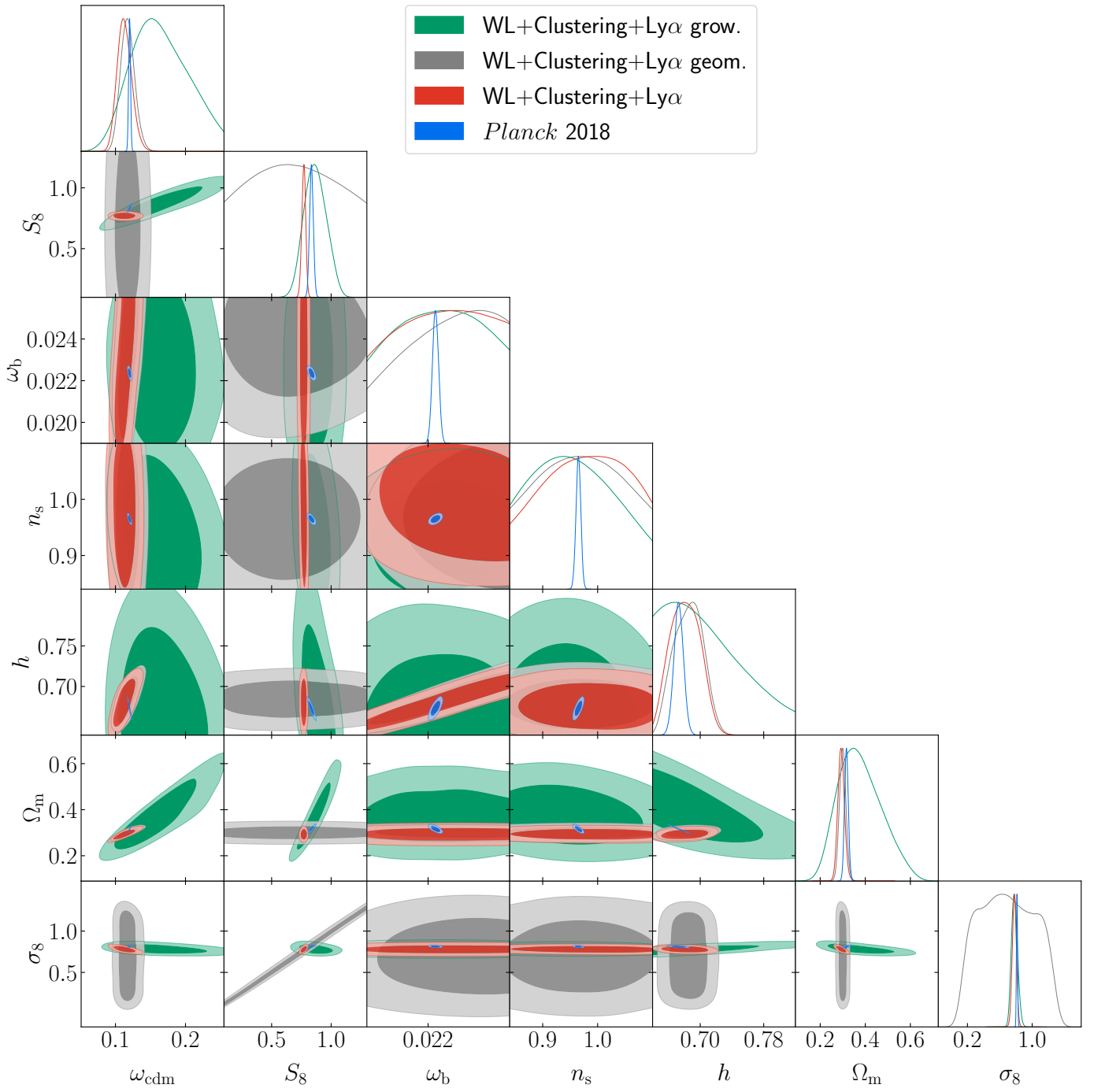
Fig. D.3. Marginalised posteriors from the analysis of the WL + Clustering + Ly-α data sets for all cosmological parameters. Each panel shows a superposition of the *growth* (green), *geometry* (grey), traditional analysis (red), and the *Planck* 2018 contours (Planck Collaboration et al. 2020a) for reference (blue).
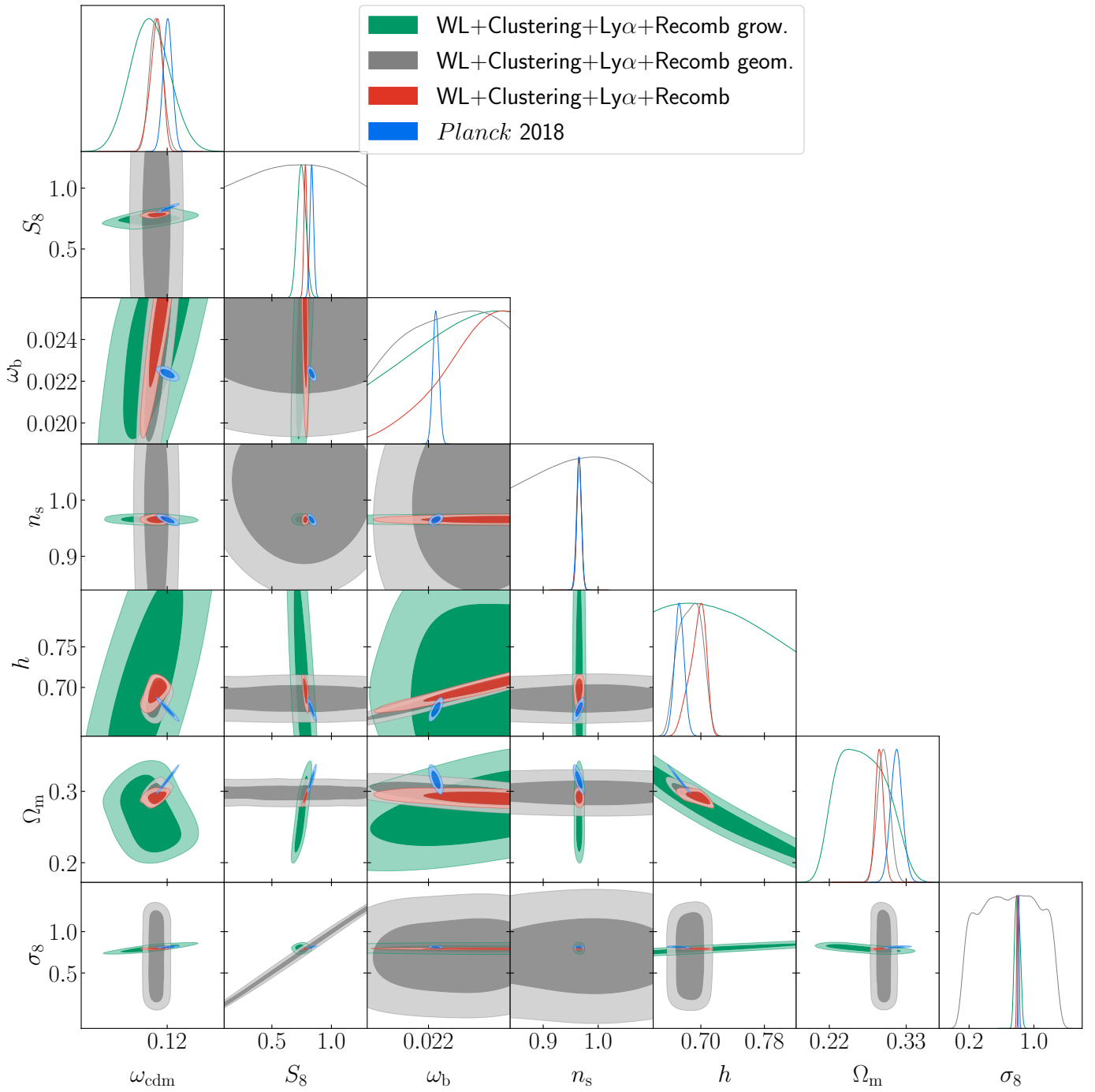
Fig. D.4. Marginalised posteriors from the analysis of the WL + Clustering + Recomb data sets for all cosmological parameters. Each panel shows a superposition of the *growth* (green), *geometry* (grey), traditional analysis (red), and the *Planck* 2018 contours for reference (blue).